AGU PUBLICATIONS

JGR

Journal of Geophysical Research: Solid Earth

RESEARCH ARTICLE
10.1002/2015JB012763

Key Points:
- The 1889 M_w 8.0-8.3 Chilik earthquake may have involved at least 175 km of rupture with measured slip of 10 m
- The earthquake may have ruptured three segments, involving both oblique left- and right-lateral slip
- The 1889 earthquake was the only surface rupture for at least 5 ka and probably for much longer

Correspondence to:
R. T. Walker,
richard.walker@earth.ox.ac.uk

Citation:
Abdrakhmatov, K. E., et al. (2016), Multisegment rupture in the 11 July 1889 Chilik earthquake (M_w 8.0–8.3), Kazakh Tien Shan, interpreted from remote sensing, field survey, and paleoseismic trenching, *J. Geophys. Res. Solid Earth*, *121*, 4615–4640, doi:10.1002/2015JB012763.

Received 21 DEC 2015
Accepted 7 MAY 2016
Accepted article online 13 MAY 2016
Published online 5 JUN 2016

Multisegment rupture in the 11 July 1889 Chilik earthquake (M_w 8.0–8.3), Kazakh Tien Shan, interpreted from remote sensing, field survey, and paleoseismic trenching

K. E. Abdrakhmatov[1], R. T. Walker[2], G. E. Campbell[3], A. S. Carr[4], A. Elliott[2], C. Hillemann[5], J. Hollingsworth[6], A. Landgraf[5], D. Mackenzie[2], A. Mukambayev[7], M. Rizza[8], and R. A. Sloan[2,9]

[1]Institute of Seismology, National Academy of Sciences, Bishkek, Kyrgyzstan, [2]COMET, Department of Earth Sciences, Oxford University, Oxford, UK, [3]COMET, Bullard Laboratories, Cambridge University, Cambridge, UK, [4]Department of Geography, University of Leicester, Leicester, UK, [5]Institute for Earth and Environmental Sciences, University of Potsdam, Potsdam, Germany, [6]Université Grenoble Alpes, ISTerre, Grenoble, France, [7]CNRS, ISTerre, UMR 5275, Grenoble, France, [8]Aix-Marseille Université, CNRS, IRD, Aix en Provence, France, [9]Department of Geological Sciences, University of Cape Town, Rondesbosch, South Africa

Abstract The 11 July 1889 Chilik earthquake (M_w 8.0–8.3) forms part of a remarkable sequence of large earthquakes in the late nineteenth and early twentieth centuries in the northern Tien Shan. Despite its importance, the source of the 1889 earthquake remains unknown, though the macroseismic epicenter is sited in the Chilik valley, ~100 km southeast of Almaty, Kazakhstan (~2 million population). Several short fault segments that have been inferred to have ruptured in 1889 are too short on their own to account for the estimated magnitude. In this paper we perform detailed surveying and trenching of the ~30 km long Saty fault, one of the previously inferred sources, and find that it was formed in a single earthquake within the last 700 years, involving surface slip of up to 10 m. The scarp-forming event, likely to be the 1889 earthquake, was the only surface-rupturing event for at least 5000 years and potentially for much longer. From satellite imagery we extend the mapped length of fresh scarps within the 1889 epicentral zone to a total of ~175 km, which we also suggest as candidate ruptures from the 1889 earthquake. The 175 km of rupture involves conjugate oblique left-lateral and right-lateral slip on three separate faults, with step overs of several kilometers between them. All three faults were essentially invisible in the Holocene geomorphology prior to the last slip. The recurrence interval between large earthquakes on any of these faults, and presumably on other faults of the Tien Shan, may be longer than the timescale over which the landscape is reset, providing a challenge for delineating sources of future hazard.

1. Introduction

This paper is concerned with the potential for large-magnitude earthquakes to occur within continental interiors, on faults that may have very low slip rates, and that are hard to discern in the geomorphology. The study of large earthquakes within continental interiors is challenging because modern examples are rare, and the interval between successive earthquakes can be very long. In consequence, instrumental seismic records do not fully represent either the full spatial extent of deformation, or the potential maximum magnitude event that is possible, and thus do not fully delimit regions at risk of future earthquake occurrence [*England and Jackson*, 2011; *Stein and Friedrich*, 2014]. Geomorphic and paleoseismic investigation of historic and prehistoric events offers the opportunity to lengthen the record of rare, large-magnitude earthquakes [e.g., *Baljinnyam et al.*, 1993; *Kumar et al.*, 2001].

We focus on the northern Tien Shan region (Figure 1), which has been relatively free from the effects of damaging earthquakes over the last hundred years, and yet the historical record [e.g., *Kalmetieva et al.*, 2009] contains a sequence of large earthquakes, in 1885 (Belovodskoe, M_s 6.9), 1887 (Verny, M_s 7.3), 1889 (Chilik, M_s 8.3), and 1911 (Chon Kemin, M_w 8.0). All caused damage in nearby population centers, including the city of Bishkek, Kyrgyzstan in 1885 (present population ~0.9 million), and Almaty, Kazakhstan in 1887, 1889, and 1911 (present population ~2 million). A recurrence of any one of these earthquakes in the future, or of similar events on other nearby structures, would result in substantial damage and loss of life.

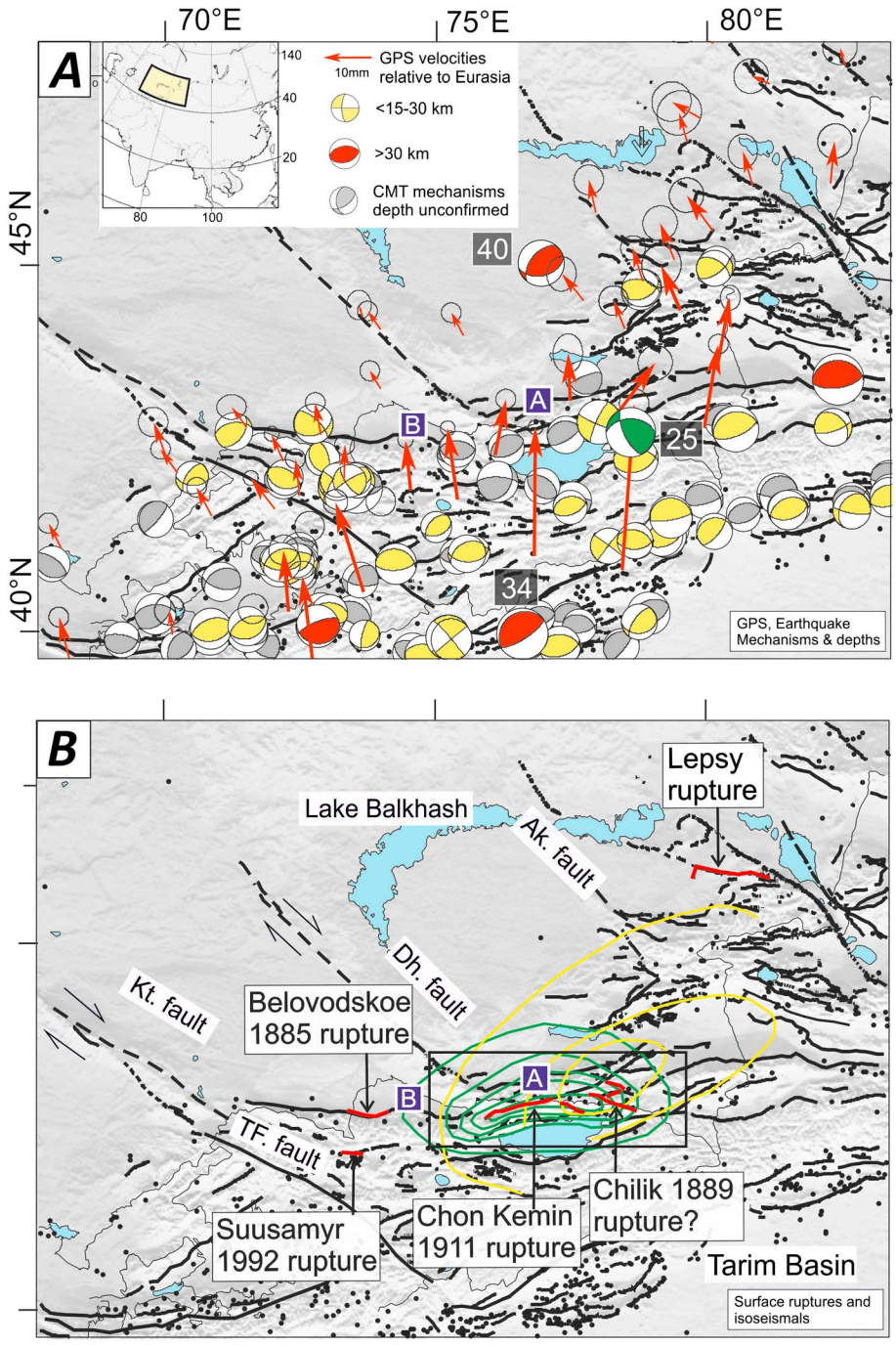

Figure 1. (a) Shaded-relief map of the Tien Shan region showing the major faults as black lines, GPS velocities relative to Eurasia as red arrows [*Zubovich et al.*, 2010], and focal mechanisms of instrumentally recorded seismicity (from the compilation of *Sloan et al.* [2011]). Those earthquakes with centroid depths greater than 30 km are shown in red, with their centroid depths labeled in each case. The focal mechanism of the 1978 Dzhalanash-Tyup earthquake is marked in green. Its depth of 25 km was reported in *Krüger et al.* [2015]. The cities of Almaty "A" and Bishkek "B" are marked. (b) Ruptures of the recent, historic, and prehistoric earthquakes mentioned in the text are shown in red. Isoseismals for the 1889 and 1911 earthquakes are shown in yellow and green (from *Arrowsmith et al.* [2015], digitized from maps drawn by *Djanuzakov et al.* [2003]).

The 11 July 1889 Chilik earthquake, with an estimated magnitude of 8.0–8.3 that has recently been supported by analysis of early seismological and magnetogram readings [*Krüger et al*., 2015], is amongst the largest continental earthquakes known, and yet its source is a continuing mystery. Although several fresh scarps have been identified in the epicentral region and inferred to result from the Chilik earthquake [*Tibaldi et al*., 1997; *Tibaldi*, 1998; *Crosby et al*., 2007], all are too short to account for the large magnitude [*Krüger et al*., 2015]. The lack of confirmed rupture poses questions as to whether slip largely failed to reach the surface, as seen, for example, in the 1992 Suusamyr earthquake in the Kyrgyz Tien Shan [e.g., *Ghose et al*., 1997; *Mellors et al*., 1997] (see Figure 1b for location), or whether some or all of the surface ruptures remain undiscovered within the steep mountainous terrain. The lack of constraint on the source of the Chilik earthquake also hampers an understanding of the relationship between the individual events in the 1885–1911 earthquake sequence, which constitutes an important archive of high-magnitude intracontinental earthquakes, with relevance to the general problem of interaction between fault ruptures.

We attempt to identify and assess the possible ruptures of the 1889 Chilik earthquake. First, we undertake detailed field investigation on the Saty fault, which was initially described by *Tibaldi et al*. [1997]. We present topographic measurements of slip associated with the Saty rupture and the interpretation of a paleoseismic site across it. We also provide radiocarbon and infrared stimulated luminescence (IRSL) age estimates for two landforms displaced by the fault. We then provide a reconnaissance of the wider epicentral region, reexamining the other fault scarps that have been put forward as potential sources of the Chilik earthquake and examining the landscape for additional fresh scarps that may have formed in 1889. As much of the Chilik valley contains steep mountainous topography, our regional survey relies primarily on satellite imagery and serves to inform future, more detailed, investigation. As such, although the fault scarps that we identify are a plausible source of the 1889 earthquake, their relationship to that event is not yet confirmed.

2. Active Tectonics and Seismicity of the Northern Tien Shan

The Tien Shan accommodate an important part of the N-S shortening between India and Eurasia [e.g., *Tapponnier and Molnar*, 1979]. There is ~22 mm/yr of N-S shortening between the Tarim basin and the Kazakh platform, of which ~6 mm/yr is accommodated across the Kazakh Tien Shan [*Abdrakhmatov et al*., 1996; *Zubovich et al*., 2010]. The shortening is accompanied by ~3–4 mm/yr of range parallel left-lateral shear, which is introduced by the clockwise rotation of the Tarim basin relative to the Kazakh platform. Deformation within the Tien Shan is accommodated on east-west reverse faults, NNW-SSE right-lateral faults, and ENE-WSW left-lateral faults (Figure 1) [e.g., *Tapponnier and Molnar*, 1979; *Thompson et al*., 2002].

Focal mechanisms of earthquakes across the Tien Shan are typically concordant with the orientations and styles of faulting as identified from the geomorphology, as described above (Figure 1). Centroid depths of $>$30 km are determined for some recent earthquakes in the Tien Shan foreland, suggesting a relatively deep seismogenic thickness [*Chen and Molnar*, 1983; *Sloan et al*., 2011; *Alinaghi and Krüger*, 2014] (see Figure 1b).

Although great earthquakes are inferred from the historical record, much of the instrumentally recorded seismicity in our study region has been moderate in size [e.g., *Chen and Molnar*, 1983; *Sloan et al*., 2011; *Alinaghi and Krüger*, 2014]. The largest event within the epicentral zone of the 1889 earthquake is the 24 March 1978 Dzhalanash-Tyup earthquake (M_w 6.9, mechanism shown in green on Figure 1b). The Global Centroid-Moment-Tensor solution for this earthquake suggests oblique shortening, with either a component of right-lateral slip on a steeply west dipping plane or left-lateral faulting on an east-west plane dipping gently to the north. *Krüger et al*. [2015] report a depth of ~25 km for this earthquake. Body waveform modeling of an M_w 5.9 event on 12 November 1990 within the Kungey Mountains west of Saty yields a centroid depth of 18 km and a mechanism with right-lateral faulting on an almost east-west plane or left-lateral faulting on an almost north-south plane.

The instrumental seismicity of our study area is important in understanding the styles of faulting and also the depth extent of faulting. To aid the interpretation of recent seismicity, we hence performed a multiple-event relocation of all events within the study area using the HDC (hypocentroid decomposition method). Full descriptions of the procedures, along with details of this particular cluster relocation, are given in Appendix A. The resulting epicenters are discussed later in the text.

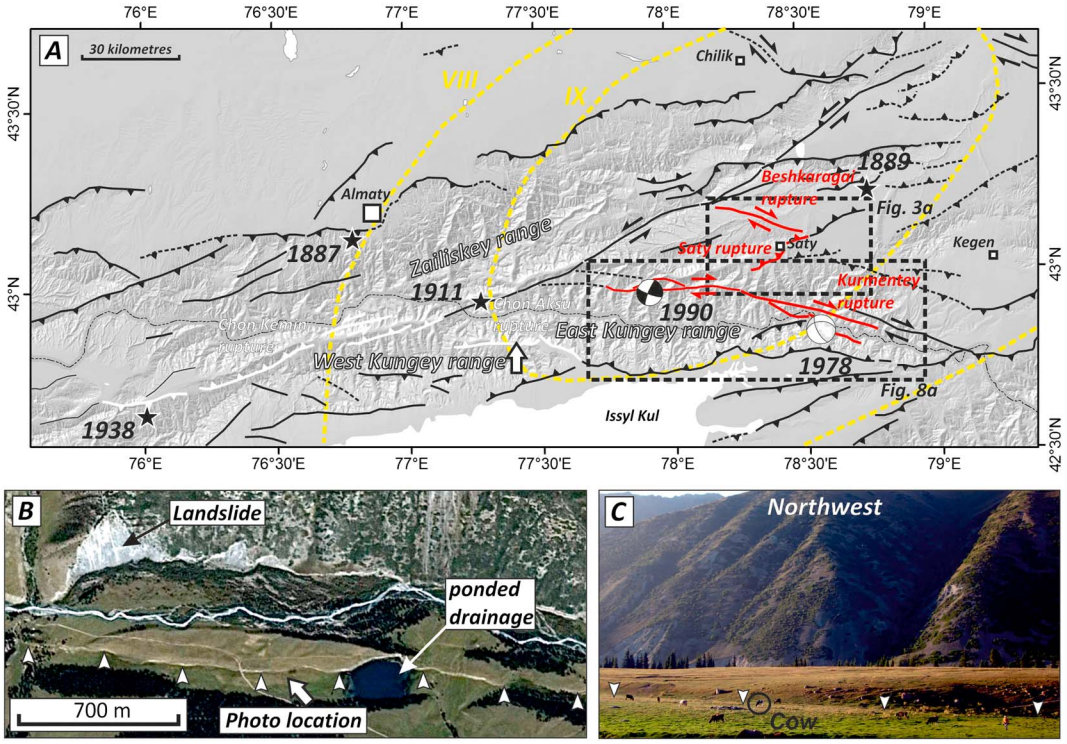

Figure 2. (a) Shaded-relief SRTM topography of the Zailisky And Kungey Tien Shan, showing the major active faults (in black, from our own mapping). Earthquake ruptures from the 1911 earthquake are shown in white, and those potentially associated with the 1889 earthquake are shown in red. The Chon Kemin and Chon Aksu ruptures of the 1911 earthquake are simplified from *Arrowsmith et al.* [2015]. The potential 1889 ruptures are from our own work, following initial observations by *Tibaldi et al.* [1997] and *Crosby et al.* [2007]. Isoseismals of the 1889 earthquake are from *Arrowsmith et al.* [2015] digitized from maps drawn by *Djanuzakov et al.* [2003]. Black stars represent the epicenters of historical earthquakes [*Kulikova and Krüger*, 2015]. The white arrow shows the location of Figures 2b and 2c. (b) Google Earth image of part of the Chon Aksu rupture. The south facing rupture is visible as a white stripe (marked by white arrows). It has uplifted the valley floor and blocked a small north flowing stream to form a pond. A landslide from 1911 is visible in the top left of the image. (c) Field photograph looking NW at the 1911 ruptures. White arrows mark the base of scarp. Scale provided by cows.

3. The 1885–1911 North Tien Shan Earthquake Sequence

The first of the 1885–1911 earthquake sequence was the 1885 Belovodsk event, which ruptured the range front of the Kyrgyz range west of Bishkek (Figure 1b). This was followed in 1887 by the Verny earthquake (estimated M_w 7.3) with an epicenter ~30 km west of Verny (the old name of Almaty) near the town of Keskelen (Figure 1b). The earthquake caused widespread landsliding within thick loess deposits along the range front [*Hay*, 1888; *Mushketov*, 1890]. No surface ruptures have yet been identified from this earthquake, and the causative fault has not been identified, although the range-front fault of the Zailisky Mountains is usually assumed.

Two years later, in 1889, the M_w 8.2 Chilik earthquake caused heavy damage in a wide region of the Tien Shan (Figures 1b and 2). A postearthquake survey of damage reports by *Mushketov* [1891] defined a macroseismic epicenter centered in the Chilik River valley, ~100 km southeast of Almaty. The survey was performed by questionnaire and did not record primary surface rupturing. The fourth event in the sequence was the 1911 Kemin earthquake (M_w 7.8–8.0), which produced ~150–200 km of ruptures along the Chon-Kemin and Chon-Aksu valleys in Kyrgyzstan (Figures 1b and 2). The seismicity in this part of the Tien Shan has continued, with further significant earthquakes in 1938 (the M_w 6.9 Kemin-Chu event), and the 1978 Dzhalanash-Tyup earthquake (M_w 6.9) [*Wilhelmson*, 1947; *Erzhanov et al.*, 1978; *Nersesov et al.*, 1981].

The ruptures of the 1911 earthquake were mapped in detail at the time [*Bogdanovich et al.*, 1914] and have been the subject of several more recent studies [*Delvaux et al.*, 2001; *Arrowsmith et al.*, 2015]. The earthquake produced a total of 145–195 km of rupture on six geometrical segments, running along both sides of the

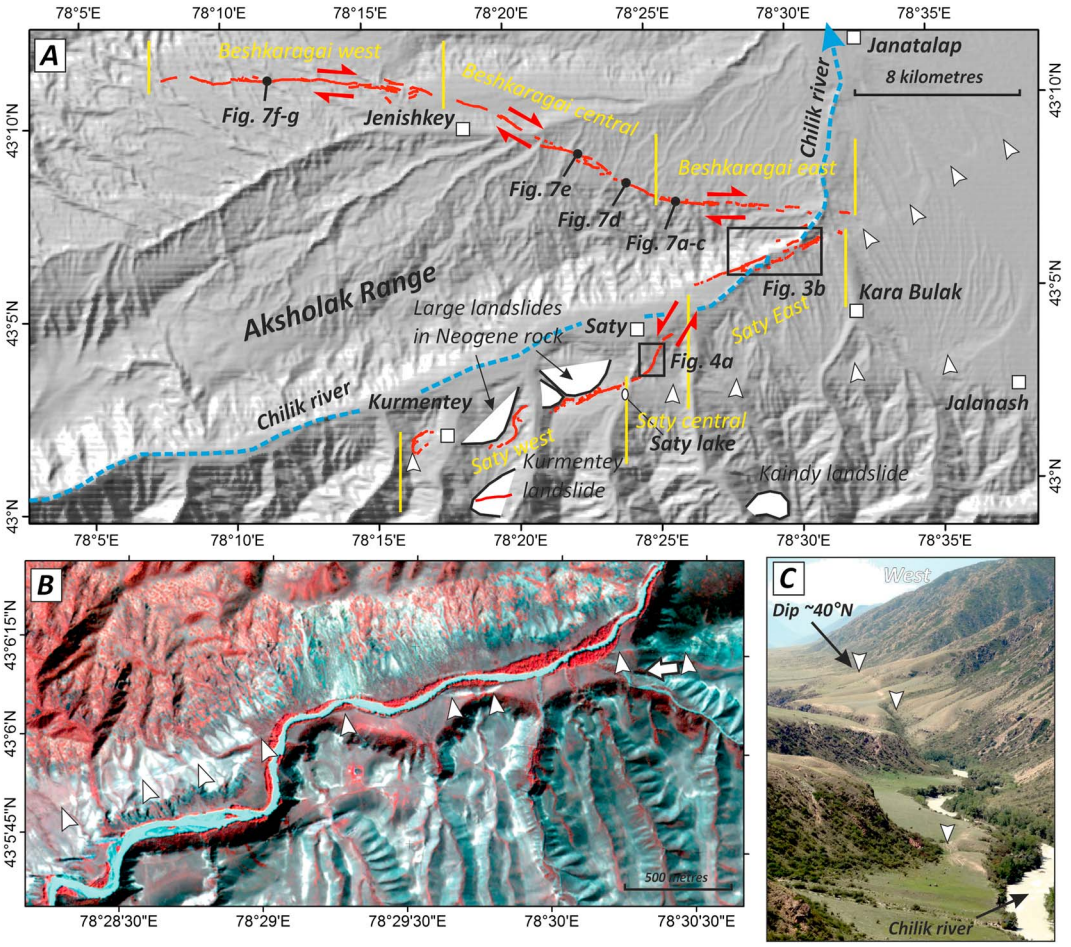

Figure 3. (a) Shaded-relief SRTM of the Aksholak Mountains and Chilik River valley, with the Saty and Beshkaragai single-event paleo-earthquake ruptures marked in red. Major landslides are marked in white. For ease of description, we separate the Saty rupture into three sections: the Saty East segment runs along the base of the Aksholak range for ~6 km, and the "Saty" section continues for another 10–15 km along the south side of the Chilik River valley. The white triangles point to eroded fault scarps that do not appear to show reactivation in a recent earthquake. The Beshkaragai fault is predominantly right lateral, though a normal component is introduced within its central section. (b) False-color KOMPSAT-2 imagery showing the east segment of the Saty rupture. The south facing scarp runs parallel to the Chilik River and is sited within the river bed for parts of its length. (c) Field photograph looking west along the Saty East rupture segment near Kara-Bulak. The angle of the rupture as it rises from the T1 to T2 terrace yields an estimated dip of ~40°N.

Chon-Kemin valley, and along the northern side of the Chon-Aksu valley (Figure 2a). The surface ruptures are identifiable in satellite imagery and in the field (e.g., Figures 2b and 2c). Although measurements of peak surface slip exceed 10 m, the average displacement is ~3–4 m. Both the Chon Kemin and Chon Aksu ruptures follow steep and narrow intramontane valleys, and the ruptures are accompanied by widespread landsliding and other mass movements. Measurements of surface displacement and length by *Arrowsmith et al.* [2015] yield a magnitude estimate of ~7.8, whereas reanalysis of contemporary seismometer recordings suggests a larger magnitude of ~8.0 [*Kulikova and Krüger*, 2015].

The magnitude of 8.3 assigned to the 1889 Chilik earthquake [*Mushketov*, 1891] is supported both by the reassessment of seismic intensities [*Bindi et al.*, 2012], and through analysis of an original seismometer record and magnetogram disturbances [*Krüger et al.*, 2015], though the latter study prefers a magnitude of ~8.0. The most intense damage was reported both on the north shore of Issyl Kul, and also in between the Chilik and Charyn rivers, with the latter assumed to be the correct epicenter as the regions close to the lake may suffer from unfavorable site effects [*Besstrashnov*, 1993, as reported in *Krüger et al.*, 2015]. Isoseismals constructed from the intensity observations reported by *Mushketov* [1891] are shown in Figures 1b and 2. They define

an epicentral zone that is elongated in the NNE-SSW direction. However, the isoseismals may be distorted by an absence of observations to the east and southeast of the epicentral region [*Besstrashnov*, 1993, as reported in *Krüger et al*., 2015]. The broad distribution of the isoseismals, combined with an absence of local intensities greater than X on the Rossi-Forel scale [*Davison*, 1921], suggests a deep focus, potentially up to ~40 km [*Bindi et al*., 2012]. The potential for deep earthquakes in the northern Tien Shan region is also suggested by centroid depths determined for some recent earthquakes, though most of the deeper seismicity occurs in the Tien Shan foreland [*Chen and Molnar*, 1983; *Sloan et al*., 2011; *Alinaghi and Krüger*, 2014], with centroid depths of earthquakes within the range interior of 30 km or less (e.g., Figure 1b). The 1978 Dzhalanash-Tyup earthquake within the 1889 epicentral zone appears to conform to this general pattern, with a depth of ~25 km from waveform analysis as reported by *Krüger et al*. [2015]. The mechanism for this event is shown in green on Figure 1b.

Given the large magnitude of the 1889 earthquake, we expect it to have produced ruptures greater in length and displacement to those identified following the 1911 event, for instance 200–300 km and 6.7–9.1 m average displacement, for thrust and strike slip, respectively, using the scaling relationships of *Blaser et al*. [2010]. Furthermore, given that the Chilik earthquake occurred only 22 years prior to the 1911 Chon-Kemin event, we would expect both ruptures to have a similar level of preservation, such that those from 1889 should still be well preserved and visible in the landscape, both in the field and in satellite imagery. However, the source of the 1889 M_w 8.0–8.3 Chilik earthquake has not been confirmed, and although several youthful fault scarps have been put forward as potential sources, all appear to be of insufficient length to account for a magnitude of $>$8. *Tibaldi et al*. [1997] suggested that ~30 km of fresh scarps along the oblique reverse left-lateral Saty fault, in the Chilik River valley, were produced in the 1889 earthquake (Figure 2a). The same authors also identified a ~40 km long zone of fresh right lateral rupturing along the Beshkaragai fault, north of the Chilik valley, which might also be related to the 1889 event (Figure 2a). Finally, *Crosby et al*. [2007] identified a 30 km long series of youthful scarps in the high parts of the Kurmentey range, which they suggested as an alternative source of the earthquake (Figure 2a). In the following sections, we reexamine each of these three fault sections, with particular emphasis on the Saty fault, as described below.

4. The Saty Fault

4.1. Morphology of the Saty Fault Scarps

Tibaldi et al. [1997] described a series of well-preserved scarps near the village of Saty in the Chilik valley (Figure 2a). The scarps occur in two east-west trending segments. The eastern segment of ~7 km length trends N080° along the margin of the Aksholak mountain range (the "Saty East" segment). The 10 km long western segment (Saty West segment, Figure 3) trends N070° on the south side of the river, between the villages of Saty and Kurmentey. Between these two segments is an ~3 km long N030° trending section, which tracks across undulating topography immediately southeast of Saty village (Saty Central Segment, Figures 3 and 4). All the scarps are steep and continuous and retain an unvegetated free face in many locations, and partially infilled fissures are preserved in the upper parts of the scarps (e.g., Figure 4). The morphology and level of preservation is typical of paleo-earthquake ruptures investigated by the authors, and by others, elsewhere in the Tien Shan and in Mongolia [e.g., *Arrowsmith et al*., 2015; *Baljinnyam et al*., 1993; *Campbell et al*., 2015; *Rizza et al*., 2011, 2015; *Walker et al*., 2006, 2015].

The northern side of the Saty fault is uplifted along its entire length. In the Saty East segment, the fault runs along the margin of Paleozoic bedrock exposure at the steep northern edge of the Chilik River valley. Along the western segment, where the fault trace runs along the southern side of the Chilik valley, a sequence of fine-grained Cenozoic basin sediments are exposed in the northern fault block (e.g., Figures 5a and 5b). The basin sediments dip gently except for within ~100 m of the scarp, where they acquire a steep dip to the north. The otherwise gentle dip of the uplifted basin sediments leads us to interpret the western segment of the Saty fault as a relatively shallow splay from the main Aksholak range-front fault. Thin slivers of Paleozoic bedrock have been exhumed immediately north of the fault adjacent to the north flowing Saty river. Exhumation of resistant Paleozoic bedrock adjacent to the Saty river has led to ponding of drainage against the bedrock scarp to form the Saty lake [*Tibaldi et al*., 1997] (Figure 2a).

Except for those regions where well-preserved late Quaternary terraces are preserved—as described below—the fault is expressed as a south facing topographic step of no more than ~50 m in height, which is visible

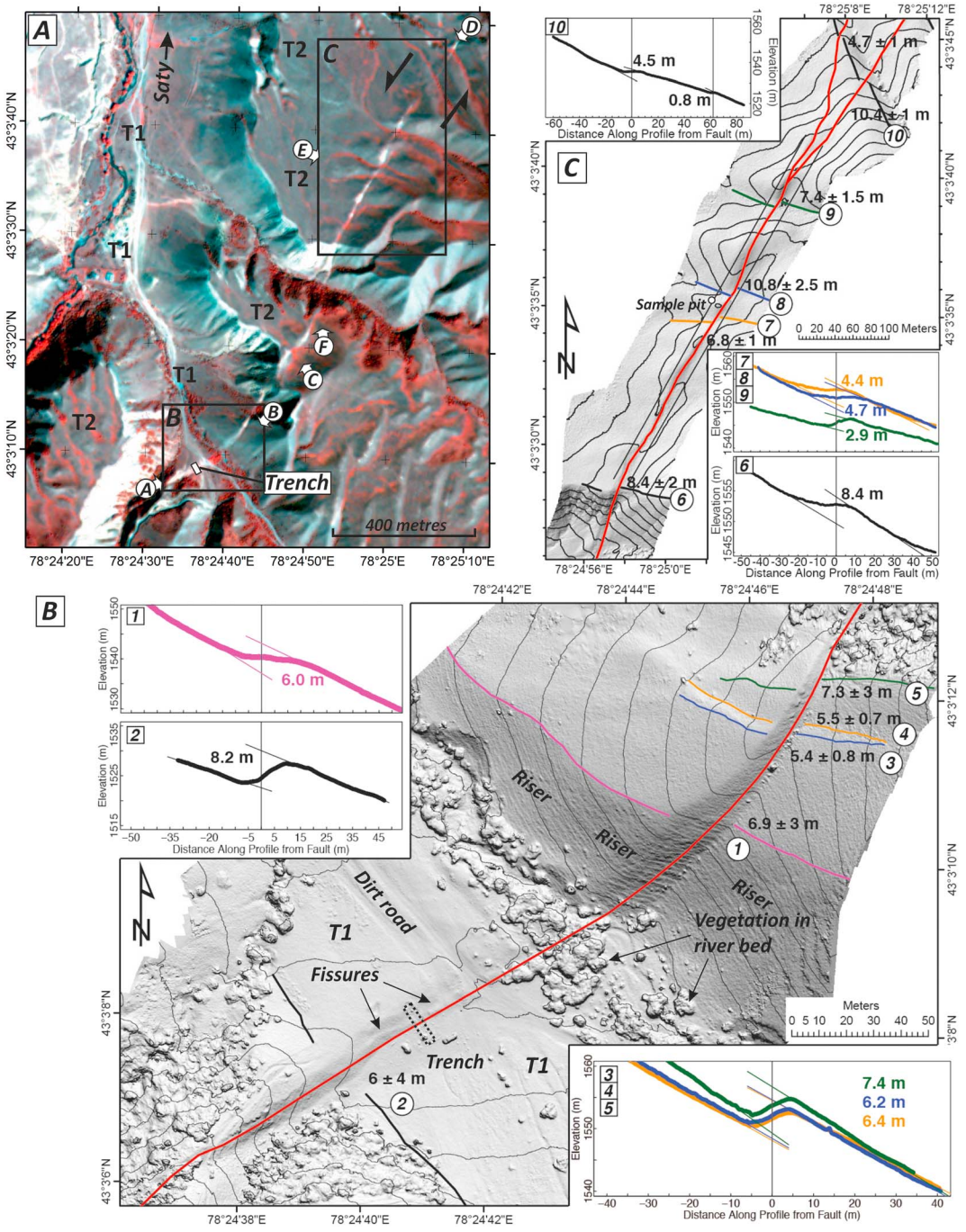

Figure 4. (a) KOMPSAT-2 false-color image of scarps ~1 km south of Saty village. The fault trends NNE-SSW in the eastern half of the image and bends to a NE-SW trend in the west. We excavated a trench across the scarp in T1 where post-earthquake sediments have ponded in front of it. (b) Digital elevation model (DEM) where the scarp crosses terrace T1. The fault bends from a strike of N050° in the southwest to a strike of N030° in the northeast. Partially infilled tension fissures are visible at the top of the scarp. Stream beds and riser margins were used as piercing lines to determine the amounts of lateral and vertical displacement. Left-lateral displacement varies from 5.4 to 7.3 m and vertical (up-to-the-north) displacement is in the range 6 to 8 m. (c) DEM showing the Saty fault as it crosses the regionally extensive T2 surface. The fault has a local strike ~ N030° in this section and appears to dip steeply to the east. Displaced piercing lines indicate left-lateral displacement of 6.8–10.8 m and 2.9–3.7 m vertical (up-to-the-west).

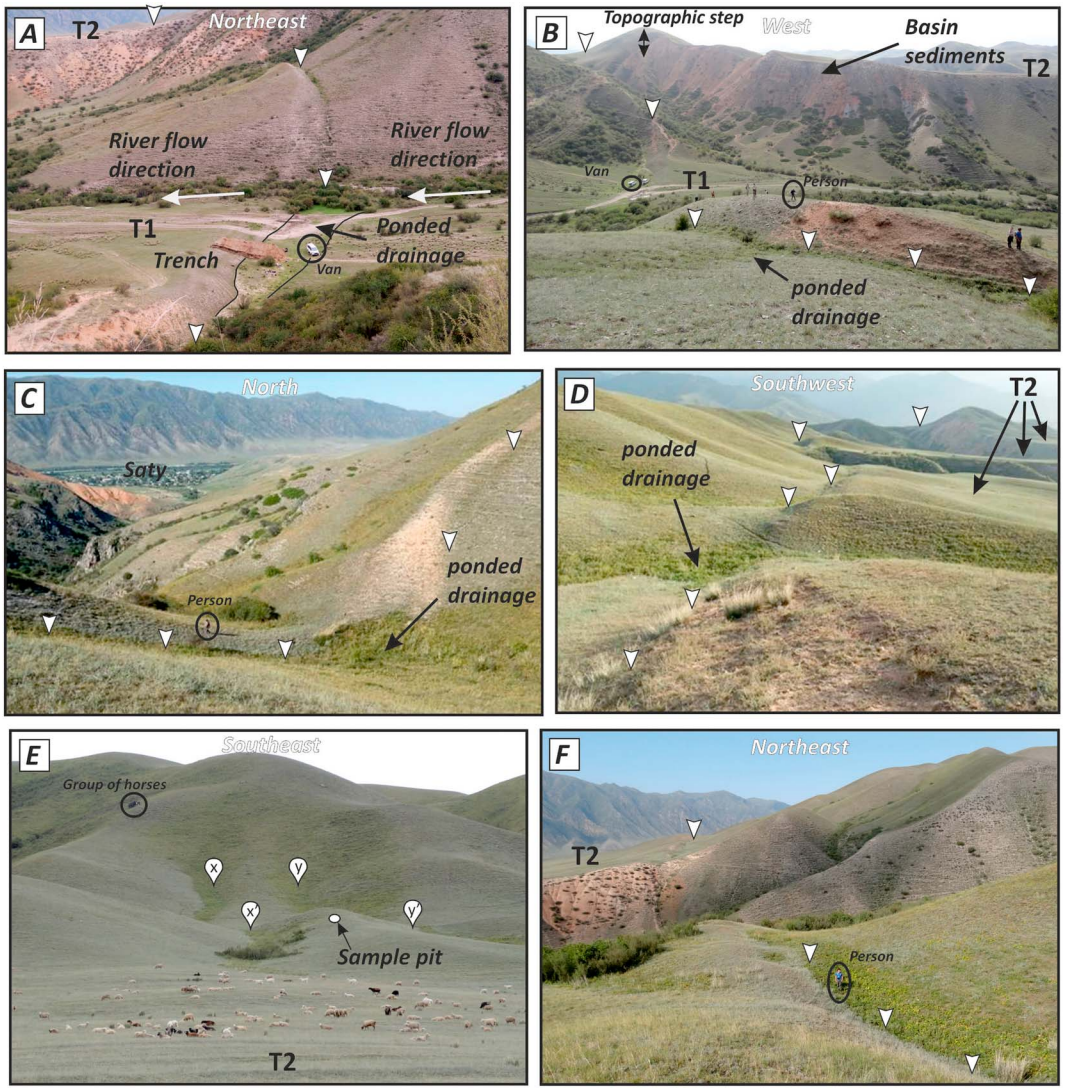

Figure 5. Field photographs of the Saty fault scarp. See Figure 4a for locations and directions of view. (a) Scarp crossing the T1 surface at our trench site. A north flowing stream was blocked by scarp formation, leading to the development of a pond. (b) Looking west along the scarp, showing the steep unvegetated scarp, and a small gully that has been blocked by scarp formation. Cenozoic basin sediments are exposed in the upthrown northern side of the fault. A topographic step of ~50 m is visible at the horizon, coincident with the fault. Our trench site, sited close to the vans, is visible in the near distance. (c) Displacement and ponding of minor drainage channel at the scarp. Saty village and the Aksholak range front are visible in the distance. (d) View southwest along the scarp showing it displacing the T2 terrace. (e) View of ~10 m left-lateral stream displacements. IRSL ages of 86–87 kyr were obtained from colluvial hillslope deposits in the sample pit indicated. (f) View northeast showing the scarp in the T2 terrace.

in the field (e.g., Figure 5b). West of the section visited in the field, a series of apparently fresh breaks are visible in satellite imagery tracking across the hillsides and following a line of youthful landslides. Additional south facing topographic steps are visible in Shuttle Radar Topography Mission (SRTM) topography for ~10–15 km along strike of the mapped eastern end of the fresh scarps (marked by white arrows in Figure 3a). We did not visit these possible fault extensions in the field, though there is no evidence for recent surface rupturing, in the form of tensional fissuring, or the presence of an unvegetated free face, along them from analysis of satellite imagery.

We performed a detailed field survey of the Saty scarps, to quantify the amount of slip across them and also to determine whether they result from a single recent earthquake. We focus on the sections of fault adjacent

Table 1. Horizontal and Vertical Displacements Measured Across the Saty Scarps[a]

		Horizontal Offset (m)			Vertical Offset (m)		
Feature ID	Feature Type	Offset	Uncertainty	Quality	Offset	Uncertainty	Quality
1	riser crest	6.9		Fair	6	0.07	Good
2	channel margin	6	4	Fair	8.2	0.06	Good
3	channel margin	5.4	0.8	Good	6.4	0.03	Good
4	stream thalweg	5.5	0.7	Good	6.2	0.04	Good
5	ridgeline	7.3	3	Good	7.4	0.05	Good
6	riser crest	8.4	2	Poor	10.4	0.07	Good
7	stream thalweg	6.8	1	Good	4.4	0.07	Good
8	stream thalweg	10.8	2.5	Good	4.7	0.06	Good
9	stream thalweg	7.4	1.5	Fair	2.9	0.04	Good
10a	riser crest (fault 1)	10.4	1	Good	4.5	0.09	Good
10b	riser crest (fault 2)	4.7	1	Good	0.8	0.03	Good
10	riser crest (total)	15.1	2	Good	5.3	0.13	Good

[a]ID numbers correspond to those on Figures 4b and 4c. Features 1–5 correspond to the T1–T2 riser, and features 6–10 are from the surface of T2.

to Saty village, where the fault has crossed to the southern side of the Chilik River and is uplifting the valley bottom (Figure 4). Here the Chilik River is flanked by two well-preserved terrace levels (T1 and T2) that are at elevations of ~10 m (T1) and ~100 m (T2) above the present main river channel. The upper terrace (T2) is widespread south of the main Chilik River and generally retains a low-relief surface. Northward flowing tributaries of the Chilik River have locally incised into T2 to form narrow river cuts. The cuts are flat bottomed and grade into the lowest terrace of the main Chilik River, on which the village of Saty is sited. This T1 surface is abandoned at the present-day, and the north flowing drainage has incised through it to grade to the current level of the Chilik River (Figure 4a).

4.2. Survey and Measurement of the Saty Scarps

To survey the ruptures we constructed a 20 cm digital elevation model (DEM) from low-altitude aerial photography using the "structure-from-motion" technique [e.g., *Westoby et al*., 2012; *Johnson et al*., 2014]. Photographs were acquired with a compact digital camera mounted on a Heli-kite (A Helium balloon with kite stabilization). A 3-D model was produced using Agisoft Photoscan software. Scale and position were assigned to the 3-D model from differential GPS measurements of ground control points placed throughout the survey area.

In Figure 4b we show the resulting DEM where the fault scarp crosses the T1 surface. In the northeast part of the image, the fault trends N030°E and displaces undulating topography associated with the riser between terraces T1 and T2, with components of both dip slip (uplift to the NW) and left-lateral strike slip. In the western part of the image, the fault bends to strike N060°E and crosses the inset fluvial terrace (T1). We identified a series of piercing lines from which vertical and lateral displacements were measured. All measured displacements are shown on Table 1, along with their estimated uncertainties. In all cases vertical uncertainties are small ($<$10 cm) because of the good linear slopes of piercing lines up and downstream.

Measurements of left-lateral displacement from the offset of stream beds, ridge crests, and terrace edges vary from 3 to 6 m. The vertical displacement appears to be relatively constant at 6–8 m, irrespective of whether the scarp is crossing the T1 surface, or the steep riser, and so the overall slip across both the T1 surface and the T1-T2 riser appears to be the same, within the uncertainties of our measurements. The relatively straight fault trace indicates a dip that is steep to near vertical (though as we show from our trenching investigation, described later, the dip shallows at the surface). This observation is consistent with those of *Tibaldi et al*. [1997], who observed a fault plane dipping 80°NNW near the Saty river gorge (e.g., Figure 2a) that placed Paleozoic rocks against Quaternary sediments. The measured components of vertical and lateral slip yield a net slip of 6.7–10.0 m on a vertical fault plane.

Figure 4c shows a DEM of the fault scarp as it crosses hillslope colluvial units at the edge of the T2 terrace surface. The fault trends N030°E and is predominantly left lateral in this section, with a component of uplift to the west that has blocked the flow of a number of minor westward flowing streams (also see field

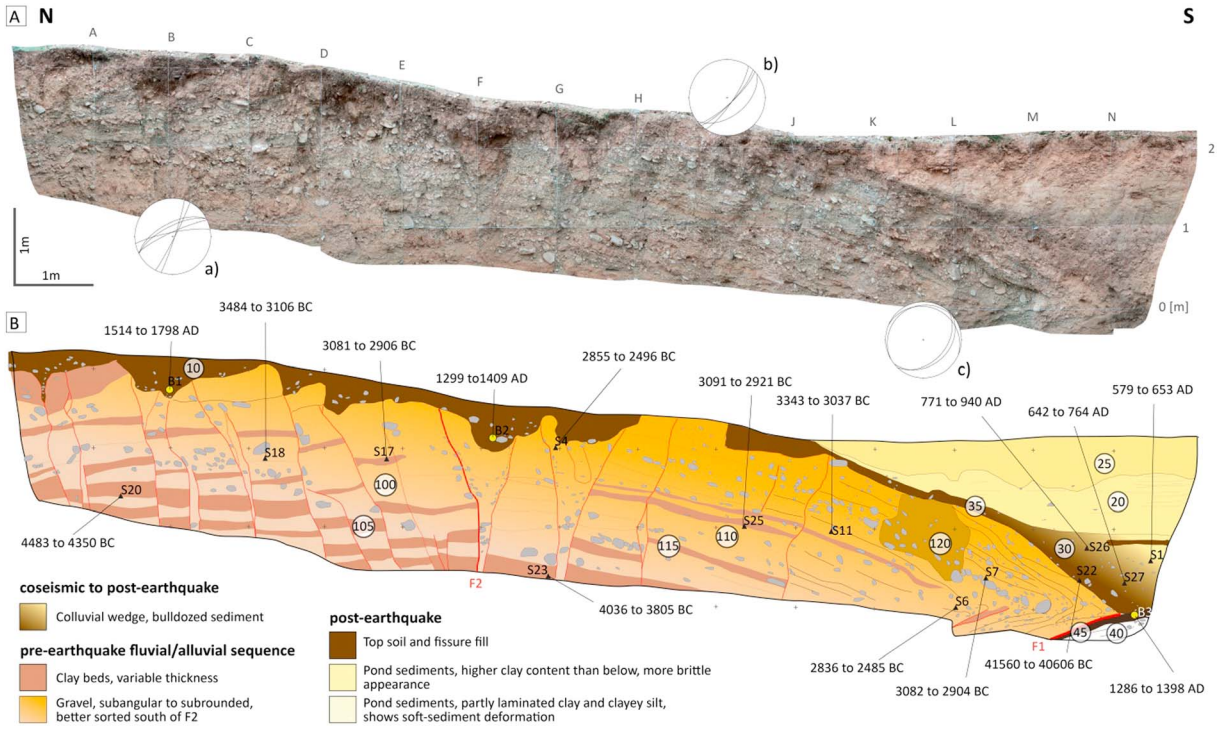

Figure 6. (a) Photomosaic and (b) log of the eastern wall of the trench. Calibrated radiocarbon ages of gastropod shells are marked by triangles. The fluvial sediments in the hanging wall date to ~5 kyr. Bulk soil samples were also dated (yellow circles) and show that the scarp buried a soil layer of calibrated age 1286–1398 A.D. Stereonets in Figure 6a are lower hemisphere projections of secondary faults and fissures ((a) north of F2 and (b) south of and including F2) and folded bedding (c) at thrust (F1) contact.

photographs, Figures 5b–5d). The interaction of the fault trace with the gently undulating topography suggests a steep dip to the east, such that the fault in this section appears to possess a slight normal component at the surface. Three stream beds show left-lateral displacements of 6.8 ± 1.0 m, 10.8 ± 2.5 m, and 7.4 ± 1.5 m and are displaced vertically by 4.4 m, 4.7 m, and 2.9 m, respectively. The three displaced stream beds on the T2 terrace yield net slip of 7.3–9.0 m, 9.5–14.1 m, and 6.6–9.4 m for a vertical fault (Table 1).

4.3. Paleoseismology of the Saty Scarps

Along the road south from Saty, the flow of a north flowing ephemeral river was blocked by formation of the scarp in the T1 surface, leading to the development of a small pond that was subsequently abandoned when the northward river flow was reestablished. We excavated a trench (~10 m long by 3 m deep) close to the road, where the fault scarp is partially buried by the postearthquake pond sediments (Figures 4b and 5a). The trench log is shown in Figure 6. Detailed lithological and structural descriptions are given in Appendix B.

4.3.1. Site Stratigraphy and Evidence for an Earthquake

We distinguished several primary units within the trench (see Figure 6, unit 10 being the youngest). Units 100 to 120 are subdivisions of the main fluvial sequence, based on secondary contacts. The exposed hanging wall is composed of coarse well-rounded fluvial gravels (units 100/110) interbedded with fine-grained silt and clay horizons (units 105/115), corresponding to the T1 terrace fan. In the northern and central part of the trench, the fluvial units are fissured and displaced along numerous fault planes, with the fissuring accommodating extension at the top of the scarp (see stereoplots in Figure 6 for orientation). Those fissures are infilled with an organic-rich dark soil. Several of the larger fissures are only partially filled and still identifiable at the ground surface (Figure 4b). Two main fissures between F and H in Figure 6 cut the entire trench depth of more than 2 m and are filled with chaotic, loose, unsorted pebbles. The fault plane defining the northern fissure (F2) has accommodated significant secondary slip, as is evident from the topographic break and the different appearance of the fluvial units north (100/105) and south (110/115) of F2. Indeed, the gravels south of F2 are generally better sorted and clay beds are thinner.

Table 2. Radiocarbon Material, Ages, and Calibration[a]

Lab code	Sample No.	Material	Stratigraphic Position	^{14}C Age (Years B.P.)	Age (Cal Years B.P.)
OX30,085	S1	shell	Postearthquake ponding (though sediments derived from scarp)	1436 ± 24	579–653 A.D.
OX30,086	S4	shell	Pre-earthquake fluvial sediment	4079 ± 28	2855–2496 B.C.
OX30,088	S6	shell	Pre-earthquake fluvial sediment	4054 ± 28	2836–2485 B.C.
OX30,089	S7	shell	Pre-earthquake fluvial sediment	4356 ± 29	3082–2904 B.C.
OX30,420	S11	shell	Pre-earthquake fluvial sediment	4484 ± 28	3343–3037 B.C.
OX30,094	S17	shell	Pre-earthquake fluvial sediment	4358 ± 27	3081–2906 B.C.
OX30,011	S18	shell	Pre-earthquake fluvial sediment	4557 ± 29	3484–3106 B.C.
OX30,009	S20	shell	Pre-earthquake fluvial sediment	5583 ± 32	4483–4350 B.C.
OX30,090	S22	shell	Postearthquake ponding (though sediments derived from scarp)	39,250 ± 290	41581–40617 B.C.
OX30,091	S23	shell	Pre-earthquake fluvial sediment	5137 ± 29	4036–3805 B.C.
OX30,092	S25	shell	Pre-earthquake fluvial sediment	4394 ± 27	3091–2921 B.C.
OX30,093	S26	shell	Postearthquake ponding (though sediments derived from scarp)	1181 ± 23	771–940 A.D.
OX30,010	S27	shell	Postearthquake ponding (though sediments derived from scarp)	1346 ± 27	642–764 A.D.
OX30,524	B1	soil	Postearthquake fissure infill	274 ± 30	1514–1798 A.D.
OX30,525	B2	soil	Postearthquake fissure infill	597 ± 27	1299–1409 A.D.
OX30,526	B3	soil	Pre-earthquake soil layer	634 ± 28	1286–1398 A.D.
OX30,095	B2-b	Amalgamated shell fragments	Postearthquake fissure infill	7527 ± 33	6457–6267 B.C.
OX30,012	B3-b	Amalgamated shell fragments	Postearthquake fissure infill	4167 ± 28	2881–2636 B.C.
OX30,013	Osl-3	Modern shell	Modern ground surface	1223 ± 25	695–884 A.D.
OX30,097	Osl-5	Modern shell	Modern ground surface	141 ± 22	1670–1944 A.D.
Beta-395370	OSL-3b	Modern shell	Modern ground surface	101.8 ± 0.4 pMC	1690–1730, 1810–1920, post 1950 A.D.
Beta-395369	OSL-3c	Modern shell	Modern ground surface	510 ± 30	1328–1445 A.D.
Beta-395367	OSL-5c	Modern shell	Modern ground surface	670 ± 30	1274–1391 A.D.
Beta-395368	OSL-5d	Modern shell	Modern ground surface	101.5 ± 04 pMC	1680–1735, 1755–1760, 1800–1935, post 1950 A.D.

[a]Samples were prepared and run at the Research Laboratory for Archaeology and the History of Art, University of Oxford. For details of the chemical pretreatment, target preparation, and accelerator mass spectrometry measurement, see Radiocarbon 46, 17-24, and 155-63, and Archaeometry 44(3, Supplement 1) and 1-149. Delta 13C values were measured independently on a stable isotope mass spectrometer (to ± 0.3 0/00 relative to Vienna Peedee belemnite). The quoted ages are in radiocarbon years using the Libby half-life of 5568 years. Calibration was performed with IntCal13: Northern Hemisphere (after *Reimer et al.* [2013]).

In the southern section of the trench, the conglomeratic fluvial units are tilted to a dip of ~30°S in the scarp itself and are drag folded along the main fault contact F1 (see stereoplot). A 20°N dipping fault plane was exposed near the base of the trench (F1 in Figure 6). Along this fault plane, the fluvial gravels from the hangingwall (120) are drag folded and overthrusted on top of a thin dark organic-rich paleosoil unit (45) and alluvial sequences (40) dipping to the north. We interpret this organic-rich layer to represent the soil horizon just before the last earthquake. The fault F1 and a part of the scarp are buried beneath the pond sediments (units 30/20/25). The base of the pond (30) is filled by polymict sediments, partly bulldozed in front of the scarp during the earthquake and at the top by granules in a silty dark-brown matrix. We interpret that unit 30 must have been fed gravitationally by materials from the free face scarp formed during or after the earthquake and the paleosoil (35) preserved at the top. Laminated clays with few granules (units 20 and 25) fill the upper section of the pond. The structures observed within the trench are typical for thrust fault scarps with hanging wall extension related to a change of fault dip as the fault approaches the surface [e.g., *Philip et al*., 1992; *Kumar et al*., 2006]. In such a scenario, the primary and secondary faults and fissures are kinematically linked. In our trench, they cut the entire fluvial sequence from top to bottom and are only covered by fissure fill and topsoil, as well as the pond sediments. This allows us to argue that within the dimensions of the trench, only one earthquake occurred and might be predated by the soil horizon (45).

4.3.2. Age Controls

Our age control comes mainly from ^{14}C dating of small terrestrial gastropod shells, which have been shown to yield reasonably accurate radiocarbon ages in North America for a range of common genera [e.g., *Pigati*

et al., 2010]. Small gastropod shells are relatively common throughout the exposed units and also at the present-day ground surface. Nine shells were taken from the deformed pre-earthquake fluvial units and yielded calibrated radiocarbon ages from ~4500 B.C. to ~2500 B.C. (samples S4, S6–7, S11, S17–18, S20, and S25; Table 2) that are in stratigraphic order. In addition, four shells (samples S1, S22, and S26–27; Table 2) were taken from sediments ponded against the scarp. All four of these shells were extracted from the lower part of the ponded sequence (unit 30 on Figure 6), and it is likely that the sediments are partially derived from the scarp and so may incorporate material that predates the earthquake. A further six modern shells were collected from the modern ground surface adjacent to the trench. These six modern shells were dated to provide estimates of the range of age offset, which can occur either due to detrital residence times in the landscape, shell secretion out of equilibrium with atmospheric carbon concentrations, or the shell carbonate not acting as a closed chemical system after burial [e.g., *Pigati et al*., 2010]. The "modern" samples (those with labels starting with "OSL" in Table 2) showed calibrated radiocarbon ages from the present to ~695–884 A.D., with two ages in the medieval period (1274–1391 A.D. and 1328–1445 A.D.), and one in the range 1670–1944 A.D. (Table 2).

We also collected bulk ^{14}C samples from organic-rich sediment overlying the top of two fissures (B1 and B2 in unit 10) and from the buried paleosoil of the footwall (B3 in unit 45). The fissure fill sediment is dated to 1359 ± 60 A.D. and 1658 ± 144 A.D. (calibrated radiocarbon ages). The buried soil, which must predate the last rupture, is dated at 1342 ± 56 A.D. Amalgamated small fragments of gastropod shell extracted from the two fissure fill bulk soil samples (B2-b and B3-b) yield much older ages of ~ 4.5 kyr and ~8 kyr.

The age offsets are critical for the interpretation of samples from the pre-earthquake and postearthquake sediments. The hanging wall units override a soil that yields a calibrated age of 1342 ± 56 A.D., and yet postearthquake pond sediments contain shells with older ages of 600–700 A.D. and that are hence out of stratigraphic order. However, we know from ^{14}C dates of modern gastropod shells at this site that inheritance of ~1 kyr is common. Also, it is likely that the lowermost ponded unit 30 incorporates older (pre-earthquake) material derived from the scarp, such that the shells extracted from it may actually be older than the sediments from which they were extracted. The paleosoil dated at 1342 ± 56 A.D. is therefore the most robust age and predates the large earthquake. Apart from the 1889 event, no other large earthquake is recorded in the last ~700 years in the Chilik valley region [e.g., *Kalmetieva et al*., 2009], and it is thus likely, though not certain, that the Saty rupture formed in the 1889 Chilik earthquake.

4.4. Time Elapsed Since the Penultimate Earthquake

The late Pleistocene geomorphic expression of the Saty fault appears to have formed in a single earthquake rupture within the last ~700 years, and yet cumulative displacements of at least 50 m in older Quaternary surfaces show that the fault was reactivated in previous slip events. Fluvial sediments at the basal layers of our trench, which are dated to 5–6 kyr, are also only affected by the most recent earthquake. The 5–6 kyr fluvial sediments are deposited as fill in the bottom of a river valley that is itself incised into an older and regionally widespread terrace (T2), which also appears to show displacement in only one event (Figures 4b and 5e). The geomorphology hence suggests that a much longer time than 5–6 kyr has elapsed since the penultimate surface slip event.

To provide constraint on the age of the T2 surface at Saty we collected two samples for IRSL (infrared stimulated luminescence) from the central section, where the slip is predominantly left lateral. The samples were collected from a 1 m deep pit excavated into a spur between two streams displaced left laterally by ~10 m. The sample pit location is shown in Figures 4c and 5e. The material within the pit was coarse colluvial hillslope deposits. All analysis procedures are described in Appendix C, and the dating results are given in Table 3. Both samples yield ages of 86–87 kyr, but as equivalent dose estimates are somewhat scattered, the age is best viewed solely as a maximum age constraint (see Appendix C). It is plausible that the T2 surface instead represents the 10–15 kyr postglacial terrace, which is widespread across the Tien Shan region [*Thompson et al*., 2002; *Landgraf et al*., 2016]. Although we are cautious in the interpretation of our IRSL ages, the fact that only one earthquake is present in the late Pleistocene geomorphology suggests that the penultimate earthquake on the Saty fault was significantly more than 5 kyr ago, and sufficiently far back in time that evidence for prior late Quaternary activity has been largely removed by erosion/deposition.

Table 3. IRSL Age Data[a]

Sample	Water (%)	Depth (m)	U (ppm)[b]	Th (ppm)[b]	K (%)[b]	Beta (ext) (μGy a^{-1})	Beta (int) (μGy a^{-1})[c]	Gamma (μGy a^{-1})	Total Cosmic (μGy a^{-1})	Total Dose Rate (Gy kyr^{-1})	CAM D_e (Gy) (n)	Age-un-corrected (ka)	Age-fading corrected (ka)
KAZ13-SATY-OSL2	2.6	0.6	3.97	10.2	2.4	2218 ± 144	802 ± 180	1485 ± 84	264 ± 13	4.77 ± 0.25	334 ± 15 (18)	70.0 ± 4.8	86.9 ± 5.9
KAZ13-SATY-OSL3	1.4	1.0	2.64	8.70	2.4	2065 ± 140	802 ± 180	1289 ± 72	250 ± 12	4.40 ± 0.24	299 ± 15 (19)	67.9 ± 5.2	86.0 ± 9.3

[a]Sample locations shown on Figures 4c and 5e. See Appendix C for full details of preparation and analytical protocols.
[b]Based on previous analyses of replicate samples using this method, 10% uncertainties were applied to U and Th and 5% uncertainties to K.
[c]Based on average attenuation factor for size range with uncertainties derived from 0.5 times the difference between the maximum and minimum grain size attenuation factor [*Durcan et al.*, 2015].

5. Evidence for Multiple Fault Rupture in the 1889 Chilik Earthquake

Accepting that the Saty scarp was generated in the 1889 Chilik earthquake, and that it follows relationships between rupture length and magnitude formulated from empirical data [e.g., *Blaser et al.*, 2010], its length of ~30 km is too short to account for the estimated magnitude of 8.0–8.3, which would require a rupture length of 200–300 km, even if the seismogenic depth was unusually large. We instead investigate the possibility that the earthquake involved rupture on more than one fault. Complex fault ruptures on multiple segments have been observed before in intraplate settings, including the 1911 Chon-Kemin earthquake of Kyrgyzstan [*Arrowsmith et al.*, 2015] (Figure 2). We therefore examine the geomorphology of the epicentral zone for additional evidence of recent surface rupturing, of a similar scale and morphology to the Saty rupture, and which might also have been caused by the 1889 earthquake. We first examine the Beshkaragai fault [*Tibaldi et al.*, 1997] and then the Kurmentey fault zone, first identified by *Crosby et al.* [2007].

5.1. The Beshkaragai Fault

The Beshkaragai rupture runs WNW for ~45 km along the northern margin of the Aksholak Mountains (Figure 3a). The fault trace is dog legged and can be subdivided into three main segments, based on variation in strike direction. The western segment trends N095° for about 20 km, the central segment trends N118° for 16 km, while the remaining eastern segment strikes on average from N090° to N095°. The rupture pattern of the fault is complex with systems of en-echelon scarps and in some places splays into several parallel branches, making slip measurements difficult. The geomorphic offsets observed on aerial images indicate a right-lateral shear and *Tibaldi* [1998] inferred that the scarp is likely to have formed recently due to its youthful appearance, reporting right-lateral offsets up to 3.5 m. Our recent survey confirms a late Quaternary surface rupture and we report that the scarp is very fresh at all points along its length, with partly unvegetated free faces preserved along it (Figure 7).

In its eastern section the rupture traverses series of shutter ridges and streams that provide well-preserved markers of displacement (e.g., Figures 7a–7c). Along this section *Tibaldi* [1998] reported a striated fault plane at one site that gave an overall N-S slip-vector azimuth and also estimated a dip of ~75°S from the way that the scarp tracks across topography, implying a reverse component of slip. At site B (see location in Figure 7b), we recorded a series of ridge crests and gullies that are all displaced right laterally by amounts of 3–4.5 m and vertically by no more than 1 m (with the southern side uplifted, Figure 7c). The remote sensing and field evidence from site B suggest a steep dip to the north (Figures 7a and 7b), such that the small vertical component may result from extension.

In its central section the fault rupture crosses a series of narrow north-south ridges and gullies that provide markers of displacement with a clear right-lateral strike-slip component and an apparent vertical offset (Figure 7d). The fault zone juxtaposes grayish Ordovician-Carbonifereous rocks to reddish Permian granodiorites [*Tibaldi*, 1998]. We map two parallel branches of the fault, separated by up to 150 m. The two parallel scarps face toward one another, forming a small graben (e.g., Figure 7d). We therefore interpret the vertical component in the central section of the fault to result from extension within a releasing bend along an otherwise right-lateral fault. From the

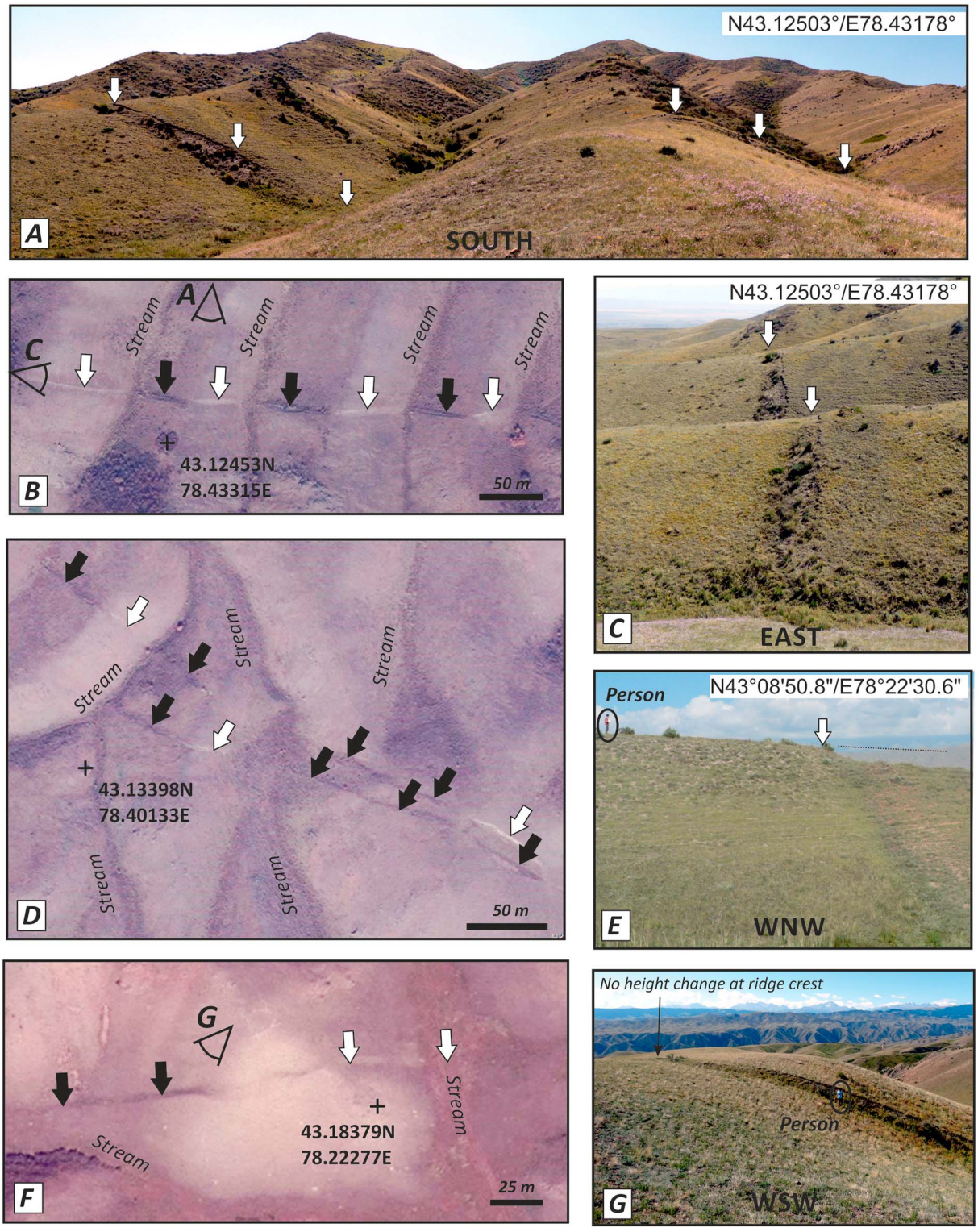

Figure 7. Satellite imagery and field views of the (a–c) eastern, (d, e) central, and (f, g) western sections of the Beshkaragai fault scarps, see Figure 3a for locations. (a) Panaromic photograph looking south at the rupture as it tracks across a series of ridges and gullies. Little vertical displacement is seen at the ridge crests of gully bases. Right-lateral displacement of the topography means that the scarp is only visible on west facing slopes. White arrows mark the visible parts of the rupture. (b) Bing Maps image of the rupture as shown in Figures 7a and 7c. North facing scarps marked with black arrows, south facing scarps marked with white arrows. (c) View east showing the steep and only partially vegetated scarps. (d) Bing maps image showing parallel scarps facing toward one another and defining graben. (e) Field photograph of the scarp within the central section. A vertical displacement of ~1 m is visible at the ridge crest. (f) Bing maps image of the western end of the rupture. (g) Field photograph from the displaced ridge shown in Figure 7f. Little vertical displacement is seen at the ridge crest, and right-lateral displacement of ~2 m is visible.

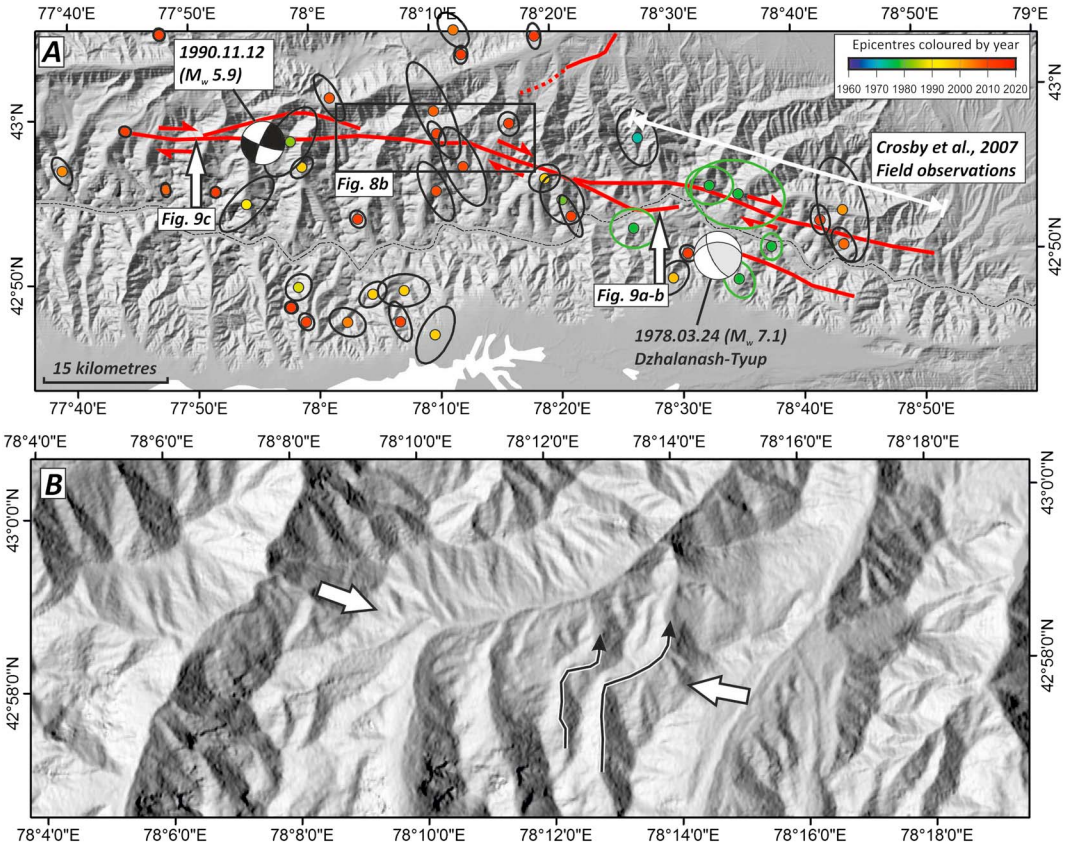

Figure 8. (a) Shaded-relief SRTM of the Eastern Kungey range with the fresh scarps of the Kurmentey fault marked in red. Calibrated earthquake epicenters are color coded by year. The main shocks of the 24 March 1978 and 12 November 1990 earthquakes are represented by their focal mechanisms. The relocation procedure has placed both events onto the mapped trace of the Kurmentey fault. The field surveys of *Crosby et al.* [2007] and the satellite views of fresh scarps presented in later panels are marked. (b) Kilometer-scale right-lateral displacement of rivers along the Kurmentey fault zone. The fault runs between the white arrows. Two small rivers that are deflected right laterally are highlighted. The larger river valleys also appear to bend to the right across the fault zone.

relationship between the fault trace and the surrounding topography, we infer that the southern fault is dipping northward with a steep fault inclination (75–80°). Offsets measured along this section are for a maximum lateral slip of ~4 m and a vertical slip of 1.5–2 m (Figures 7d and 7e).

We define the western section of the Beshkaragai fault as the part west of Jenishkey village (Figure 3a). We examined only one short part of the western section, as shown in Figures 7f and 7g. Here the fault trends roughly east-west and has right laterally displaced a series of ridges and gullies. The fault scarp is steep and unvegetated and appears similar in morphology to the more easterly sections, and yet the amount of displacement is smaller. The amount of strike slip was measured in the field at ~2 m (see person for scale in Figure 7g). The ridge crest in Figure 7g is not displaced vertically, such that the slip appears to be almost pure strike slip.

5.2. The Kurmentey Fault

The Eastern Kungey range bounds the northeastern shore of the Issyl Kul lake to the south and the Chilik River valley to the north (Figures 2 and 8a). The range is ~150 km in length and is asymmetric, with a main drainage divide located close to the southern range front. Active faulting along the southern range front is predominantly reverse, as shown in the Chon-Aksu rupture of the 1911 Chon-Kemin earthquake, which broke the westernmost ~50 km of the fault [*Bogdanovich et al.*, 1914; *Delvaux et al.*, 2001; *Arrowsmith et al.*, 2015]. The narrow Chon-Aksu valley is bounded by the Western and Eastern Kungey ranges, which are aligned in a left-stepping en-echelon arrangement [*Selander et al.*, 2012]. We describe the Kurmentey fault, which is a right-lateral fault zone cutting through the high mountainous interior of the Eastern Kungey range.

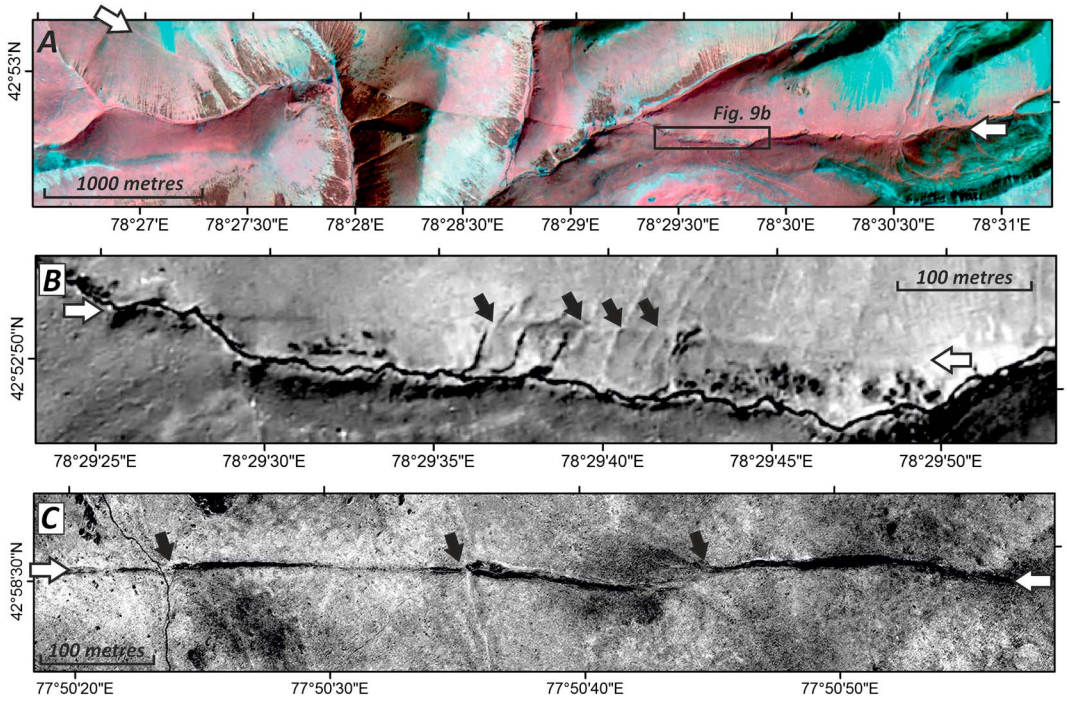

Figure 9. (a) False-color KOMPSAT-2 imagery of the Kurmentey fault close to the main drainage divide of the Eastern Kungey range. (b) Panchromatic KOMPSAT-2 image (1 m pixels) showing a detail of the Kurmentey scarps. The scarp is in shadow (north facing) on a west facing hillslope and in sunlight (south facing) on an east facing hillslope, indicating right-lateral displacement of topography. A series of small south flowing streams appear to be displaced right laterally by ~8 m. (c) Right laterally displaced stream beds (marked by black arrows) and interfluves along the western part of the Kurmentey fault.

Crosby et al. [2007] mapped ~30 km of fresh fault scarps within the southeast Eastern Kungey range from aerial photographs and performed reconnaissance visits at a number of locations (R. Arrowsmith, personal communication, 2015) (see Figure 8a for mapped region). The authors suggested the scarps may be related to the 1889 earthquake on the basis of their freshness. From a remote sensing survey we identify westward continuations of these scarps for a length of at least ~100 km through the high mountainous interior of the Eastern Kungey range. We mapped the ruptures as far west as longitude ~77°45′E (Figure 8a), though we do not rule out that they continue beyond that point. The scarps are difficult to access in the field due to the high mountainous topography, but from our interpretation of satellite imagery we suggest that the slip is oblique right lateral with a component of uplift to the south.

We show two examples of the Kurmentey scarps in Figure 9. The first example (Figure 9a) is from the Kazakh-Kyrgyz border region at longitude 78°30′E, within the section identified by *Crosby et al*. [2007]. The scarps are relatively straight as they track across high mountainous topography, though slight deflections to the south as they cross high ridges indicate a steep dip to the north. A right-lateral strike-slip component is apparent in the close-up view in Figure 9b, where the scarp is in shadow on west facing slopes, but in sun on an east facing slope, indicating right-lateral displacement of topography. A series of small spring-fed streams in the central part of Figure 9b appear to have been deflected in a right-lateral sense by ~8 m.

Fresh fault scarps are also visible in the steep topography of the western part of the Kurmentey fault zone. In Figure 9c an east-west scarp tracks across an undulating hillside, crossing several southward flowing stream beds (marked by black arrows) and interfluves. The fault trace is deflected slightly northward in the gullies (stream beds marked by black arrows), suggesting a steep northward dip. The image shows that although the scarp is in shadow at all points, the scarp height varies, being larger on west facing slopes than on east facing ones. The variation of scarp height indicates components of both vertical (up-to-the-south) and right-lateral displacement across the scarp.

The Kurmentey fault zone has not previously been identified as a single through-going structure. However, we note that right-lateral displacements, along the line of fresh scarps described in the previous paragraphs,

are apparent in the deflection of the large river systems by amounts varying from 0.4 km to >1 km (Figure 8b). There is also instrumental seismic evidence for strike-slip faulting within the Kungey range, with two significant strike-slip earthquakes within the Eastern Kungey Mountains over the past decades (Figure 8a). The first of these is the 1978 Dzhalanash-Tjup (M_w 6.9) earthquake, which has nodal planes indicating either right-lateral slip along an east-west plane or left-lateral faulting on a north-south plane. The calibrated location of the 1978 earthquake (Appendix A) is at the eastern end of the zone of fresh scarps that we described above, on the southern of the two parallel scarps that are mapped at this longitude. These scarps are visible in pre-earthquake CORONA imagery and so have formed prior to the 1978 event. As *Krüger et al*. [2015] report a depth of 25 km for the 1978 earthquake, the alignment of its epicenter with one of the mapped surface traces does not necessarily suggest a structural connection. An M_w 5.9 event in 1990 is relocated on the trace on the Kurmentey fault close to the western end of the mapped fresh scarps. The focal mechanism obtained from waveform modeling [*Sloan et al*., 2011] indicates right-lateral faulting along an east-west plane with a centroid depth of 18 km. A number of smaller earthquakes in the region show a broad alignment along the Kurmentey fault. A second small cluster of seismicity occurs immediately north of the Issyl Kul shoreline, in the hanging wall of the Chon Aksu fault (Figure 8a).

6. Discussion

We have described 175 km of well-preserved fault scarps within the epicentral zone of the 1889 Chilik earthquake (Figure 2). The ruptures are on three separate faults, which are arranged in a "z" shape and have slip that varies between oblique left-lateral slip on a WSW-ENE trend, to right-lateral slip on a WNW-ESE trend. Such a pattern, though unusual, is compatible with the overall ~N-S shortening across the northern Tien Shan [*Tapponnier and Molnar*, 1979; *Campbell et al*., 2013], and rupture in conjugate left- and right-lateral faults in a single earthquake is known from other examples [e.g., *Elliott et al*., 2012; *Rizza et al*., 2015]. Nonetheless, the multifault rupture that we infer for the 1889 earthquake would not pass several of the filters applied in the most recent "Earthquake Rupture Forecast" for California [*Field et al*., 2014], such that if we are correct, it has implications for the modeling of hazard.

The Saty scarps have a combined length of up to 30 km and involved net oblique reverse left-lateral slip of ~10 m. The right-lateral Beshkaragai scarp has a length of ~45 km and a maximum right-lateral slip of 4.5 m. The right-lateral Kurmentey scarps, for which we only have observations from satellite imagery, appear to extend for ~100 km. Relatively large strike-slip displacements of at least 8 m appear to be visible on the Kurmentey fault in satellite imagery, though in this case we have no field verification that these displacements result from a single earthquake. Along the Saty fault we have confirmed through paleoseismic trenching that the scarp was formed in a single earthquake, within the last 700 years, and with ~10 m of slip.

The 1889 Chilik earthquake has an estimated magnitude of 8.3, assigned from contemporary damage reports [*Mushketov*, 1891], recently reassessed at 8.3 + 0.2/−0.1 [*Bindi et al*., 2012]. Reanalysis of seismic records yields a magnitude in the range 8.0–8.3, with a preferred value of 8.0 [*Krüger et al*., 2015]. From empirical scaling relationships based on global earthquakes [e.g., *Blaser et al*., 2010], we would expect surface rupture lengths of 200–300 km for an earthquake of this size, and average surface slip between 6.7 and 9.1 m, for thrusting and strike slip, respectively. Given the scale of the ruptures, it is therefore plausible that all of the scarps that we have described were formed in a single earthquake of magnitude ~8. The scarps that we have described occur on three discrete faults; the Saty and Beshkaragai ruptures are separated by only ~2 km at their eastern end. The mapped Saty and Kurmentey ruptures are separated by a larger distance of 6–7 km, greater than the 4 km width that is typically thought to prevent rupture propagation [*Wesnousky*, 2006]. However, the multisegment rupture of the 1911 Chon-Kemin earthquake, immediately west of the Chilik earthquake zone, also appears to have jumped across a step over > 10 km in width [*Arrowsmith et al*., 2015]. The 175 km rupture length is relatively short to account for the 8+ magnitude. It is possible that slip extended to depths of ~40 km [*Bindi et al*., 2012; *Krüger et al*., 2015], which is larger than what is typical for continental regions, and would produce a correspondingly larger area of rupture. It is also possible that the peak slip was much larger than we have measured in the few places investigated in the field. For instance, *Manighetti et al*. [2007] suggest that immature faults, such as those we have described, tend to fail in "energetic" ruptures with large slip to length ratios. Alternatively, the relatively short mapped rupture length may mean that additional fault ruptures remain undiscovered.

Each of the ruptures follows geological faults, and topographic disruptions are visible along them, including kilometer-scale lateral deflections attesting to relatively large amounts of slip. It is, however, striking that all three fault sections do not appear to be superimposed on preexisting scarps within late Pleistocene alluvial cover. Our best constraint on the minimum time elapsed since the penultimate surface-rupturing earthquake is from Saty, where fluvial sediments at the basal layers of our trench, which are dated to 5–6 kyr, are only affected by the most recent earthquake, which occurred in the last 700 years. These fluvial sediments predate the abandonment of a fluvial terrace that is itself incised into an older and regionally widespread terrace for which our two IRSL ages provide an upper age limit of ~85 kyr. Pending further work these ages are interpreted cautiously as maximum age constraints. Notwithstanding we infer that the penultimate earthquake on the Saty fault was significantly more than 5 kyr ago, and sufficiently far back in time that evidence for prior late Quaternary activity has been largely removed by erosion/deposition.

The scenario that we have presented for the source of the Chilik earthquake, in which a large-magnitude earthquake occurs on a fault (or faults) that have little prior geomorphic expression, is not unique for large earthquake ruptures within continental interiors [e.g., *Quigley et al*., 2012; *Walker et al*., 2013; *Elliott et al*., 2015; *Walker et al*., 2015]. The 2010 (M_w 7.1) Darfield earthquake in New Zealand, in particular, involved rupture on multiple fault segments with a wide range of strike and rake and with little prior geomorphic expression [e.g., *Elliott et al*., 2012; *Quigley et al*., 2012]. Paleoseismic trenching on the main strike-slip fault strand revealed a penultimate event at 20–30 ka, whose scarp had been completely eroded and buried by later alluvial deposits [*Hornblow et al*., 2014]. In Kazakhstan, a prehistoric example is provided by *Campbell et al*. [2015], who describe field evidence for rupture in a previously unknown large earthquake (within the last ~350 years, estimated magnitude of ~7.8–8.2) within the Tien Shan foreland close to the town of Lepsy (Figure 1b). Along its western half, the Lepsy rupture tracks across open steppe with no evidence for prior fault movement other than a ~2 m scarp that the authors infer to result from an earthquake at ~4–6 kyr.

Irrespective of whether the scarps on the Kurmentey, Saty, and Beshkaragai faults occurred during the 1889 Chilik earthquake, in an earlier unrecorded event, or in separate smaller (though necessarily high stress drop) events, their very existence shows that major earthquakes have occurred within 100 km of the city of Almaty on faults that show little evidence for prior late Quaternary activity. The last century has seen unprecedented growth in the urban populations in the continental interior of Asia, much of this growth occurring in the face of poorly constrained earthquake hazard, and many recent destructive earthquakes within continental interiors have occurred on faults not previously recognized as active in the late Quaternary [*England and Jackson*, 2011].

The realization that large earthquakes deep within continental interiors, even in known deforming zones such as the Tien Shan, can occur on slow moving and hard to identify faults highlights a need to focus scientific study on earthquake hazard in intraplate regions, where the interval between destructive earthquakes may be much longer than the historical record.

7. Conclusions

Our reconnaissance study indicates that the great Chilik earthquake of 1889 ruptured a series of discrete faults, each with relatively small cumulative geological displacement and with recurrence intervals that are sufficiently large to remove most evidence for prior late Pleistocene activity upon them. It is the pristine environment of central Asia that has allowed us to identify, map, and characterize these candidate ruptures from this important historic earthquake directly from their expression in the landscape. The cumulative length of these ruptures is ~175 km, which is rather short considering the 8+ magnitude of the Chilik earthquake. It is possible that the large magnitude results from an abnormally deep seismogenic thickness (~40 km). Additionally, parts of the surface rupture may remain undiscovered.

Appendix A: HDC Relocations

We used a HDC (hypocentroidal decompositional algorithm) earthquake relocation technique extensively described elsewhere [e.g., *Ritzwoller et al*., 2003; *Bondár et al*., 2004; *Tatar et al*., 2007; *Roustaei et al*., 2009; *Walker et al*., 2011; *McNamara et al*., 2014] to determine the epicentral locations of 78 earthquakes in the vicinity of the earthquake ruptures. These earthquakes occurred between 1965 and 2012.

Unknown variations in velocity structure along teleseismic ray paths lead to large uncertainties in *absolute* hypocenter locations. Multiple-event relocation techniques exploit the fact that phases from clusters of nearby earthquakes will travel along similar paths to a distant seismometer and so should sample a similar velocity structure. By considering relative arrival times of these phases much tighter constraints can be placed on the *relative* hypocenter locations [*Jordan and Sverdrup*, 1981].

The method used frames the relocation as two independent problems. The first is the production of a set of relative hypocentral locations (in the form of cluster vectors from the hypocentroid—the geometrical mean of the locations and origin times). This is done by considering traveltime difference using all available catalog-derived data regardless of phase or station distance. Second is the inversion for the absolute values of location and origin time for this hypocentroid using a subset of the available phase data, chosen to limit the effect of uncertainties in velocity structure. In this case we use only stations within the immediate vicinity of the cluster ($<$1.25°) and only direct arrivals. Over this relatively small area lateral variations in velocity may be expected to be reasonably small and, due of the short distance traveled, will have a limited effect on arrival times. One of the advantages of this technique is that it allows the relative location of earlier events to be well determined by a sparse teleseismic network and the absolute location to be determined using the relatively dense regional network available for more recent events.

Arrival time data are weighted using empirical read errors calculated from the misfit of all instances of each station-phase pair within the data set. These empirical read errors are also to iteratively identify and eliminate outliers, until all of the readings used are statistically consistent with the observed spread of residuals ($\pm 3\sigma$).

While there are a reasonable number of stations within 1.25° of the cluster, there is only limited amount of data from stations immediately above the events. Without stations in the immediate epicentral area, there is little control on source depth, due to the well-known trade-off between depth and origin time. For this analysis we have fixed the depths of the cluster event at 22 km (based on catalog depth phases and probably close to the base of the seismogenic layer in this area) [*Sloan et al.*, 2011]. This likely does not represent the true depth of all of the events, but while this will result in deviations from the true origin time (as noted above) this should have little effect of the earthquake epicenters. We experimented with changing the depths of five individual events for which a reasonable number of depth phases had been reported and which showed significant misfit to the expected arrivals predicted for our fixed cluster depth. This resulted in a maximum depth change of -6 km but did not significantly change the resulting epicentral locations (Table A1).

Appendix B: Detailed Trench Descriptions

Six main units can be distinguished in the trench (eastwall).

Unit 10 (topsoil and fissure fill, postearthquake): very irregular lower boundary, loose, dark-brown soil, rich in organics, heavily penetrated by small roots of grasses. This unit thickens and fills the small graben structures and thins above the gravel. The topsoil is only developed above the hanging wall units and does not cover the pond. *Samples*: B1 and B2 (bulk soil from fissure fill and radiocarbon).

Unit 20 (the pond, postearthquake): the ponded sediment yields beige to yellow, partly laminated clay and silt with carbonate content (reacts to HCl). In places, small-scale soft-sediment deformation is observed, possibly indicating either further seismic shaking during sedimentation or high sedimentation rates. The pond deposits differ in the lower and upper parts, but the transition is gradual, the contact undulated. Toward the top, the clay content increases in lenses and the clay has a more brittle appearance (25). The sediments onlap the scarp upward, abolishing much of the vertical fault offset. The top of the pond shows no soil development, but few plants and grasses grow and their roots penetrate the uppermost centimeters. Maximum observed thickness in the trench reaches 140 cm.

Unit 30 (colluvial wedge, bulldozed sediment, postearthquake): This bulldozed sediment is wedge shaped, in total up to 1 m thick, and contains unsorted gray-brown mottled clay with few clasts. The sediment does not react to HCl. Its upper contact is irregular and interfingers with the pond sediment (unit 20/25). The lower contact is also irregular but clearly to distinguish from the clast-supported unit of granules and pebbles (unit 110) below. *Samples*: S1, S22, S26, and S27 (snails and radiocarbon).

Table A1. Earthquake Locations Obtained Through the HDC Location Technique

Date	Origin Time	Latitude	Longitude	Magnitude	Magnitude Type	Magnitude Source	First Semiaxis (deg)	Length (km)	Second Semiaxis (deg)	Length (km)	Area (km^2)
1965-11-07	18:06:32	43.133	78.433	4.7	Mb	ISC	72	2.23	162	2.94	20.6
1967-11-30	11:44:39	42.964	77.457	4.8	Mb	ISC	309	2.23	39	2.41	16.9
1972-12-24	11:24:15	42.970	78.449	4.6	Mb	ISC	73	2.39	163	3.43	25.8
1975-02-12	13:34:54	43.199	78.832	5.3	Mb	ISC	60	1.77	150	1.97	10.9
1978-03-24	21:05:46	42.848	78.552	6.1	Mb	ISC	298	1.42	28	1.74	7.8
1978-03-25	02:25:18	42.824	78.580	4.8	Mb	ISC	66	1.96	156	2.44	15
1978-03-25	06:28:02	42.909	78.583	4.7	Mb	ISC	14	3.91	104	5.39	66.3
1978-03-26	08:51:23	42.855	78.626	4.9	Mb	ISC	280	1.6	10	1.83	9.2
1978-03-26	22:59:40	42.879	78.439	4.5	Mb	ISC	4	2.44	94	2.82	21.6
1978-03-30	04:00:01	42.919	78.545	4.7	Mb	ISC	357	2.37	87	2.85	21.2
1981-08-30	04:04:49	42.911	78.343	4.4	Mb	ISC	60	2.47	150	3.17	24.6
1982-12-31	19:46:45	42.883	77.395	5.7	Mb	ISC	309	1.24	39	1.41	5.5
1983-03-13	12:20:13	43.285	77.445	4.7	Mb	ISC	62	1.9	152	2.39	14.3
1983-09-27	05:10:02	42.979	77.975	4.1	Mb	NEIS	304	2.43	34	4.51	34.5
1986-01-25	16:00:40	43.150	77.417	5.1	Mb	ISC	315	1.3	45	1.57	6.4
1986-07-17	08:15:34	43.306	78.014	4.4	Mb	ISC	74	2.12	164	2.53	16.8
1987-05-26	13:44:19	42.833	77.979	4.6	Mb	ISC	316	1.68	46	1.97	10.4
1987-09-20	03:54:04	42.938	77.606	4.6	Mb	ISC	290	1.44	20	1.78	8.1
1988-06-17	13:30:43	42.965	77.442	5.2	Mb	ISC	314	1.24	44	1.51	5.9
1990-11-12	12:28:51	42.979	77.937	4.9	Mb	ISC	308	1.26	38	1.54	6.1
1990-12-28	00:26:14	42.918	77.912	4.4	Mb	ISC	316	1.89	46	4.2	25
1992-02-25	09:30:54	43.207	78.032	4.4	Mb	ISC	291	2.03	21	3.1	19.7
1996-05-11	10:32:47	42.933	78.320	4.1	Mb	ISC	329	1.76	59	2.16	12
1996-12-16	06:59:51	42.823	78.080	4.3	Mb	ISC	322	1.57	52	2.08	10.3
1996-12-16	07:00:13	42.780	78.163	4.4	Mb	ISC	299	1.99	29	3.63	22.7
1996-12-24	19:15:54	42.826	78.122	3.7	Mb	ISC	358	2.12	88	3.1	20.7
1996-12-28	07:40:32	42.953	77.989	4.4	Mb	ISC	319	1.4	49	1.86	8.2
1997-07-09	16:24:54	43.103	78.317	3.8	Mb	ISC	306	2.97	36	4.23	39.5
1998-04-26	17:09:54	42.828	78.490	3.6	Mb	ISC	313	1.78	43	2.47	13.8
2002-03-26	04:32:33	42.889	78.725	3.9	Mb	ISC	79	2.88	169	6.07	54.9
2003-06-18	12:48:15	42.921	77.191	3.5	Ml	KNET	31	1.6	121	3.08	15.5
2003-07-20	00:46:53	42.921	77.421	2.6	Ml	KNET	44	1.61	134	2.95	15
2003-09-19	00:13:41	42.957	77.661	3.8	Mb	ISC	63	1.44	153	2.02	9.1
2003-12-31	09:44:54	43.027	77.416	3.9	Mb	ISC	43	1.46	133	2.09	9.6
2004-01-30	10:07:51	42.796	78.044	3.8	Mb	ISC	22	1.88	112	2.36	13.9
2004-05-13	14:21:21	42.951	77.482	3.1	Ml	KNET	43	1.74	133	3.43	18.8
2005-06-24	09:33:21	42.990	77.200	4.4	Mb	ISC	37	1.39	127	1.64	7.1
2005-08-03	04:26:32	43.085	78.203	3.4	Ml	KNET	55	1.74	145	2.51	13.7
2005-08-16	17:21:02	43.376	77.485	4.4	Mb	MOS	57	2.49	147	5.84	45.8
2005-10-09	12:00:29	43.184	77.311	4.4	Mb	ISC	36	1.36	126	1.92	8.2
2006-03-02	22:24:16	42.854	78.725	3.8	Mb	ISC	66	1.63	156	2.29	11.7
2006-06-23	19:43:08	42.907	77.447	2.4	Mb	NNC	45	1.75	135	3.06	16.8
2006-10-22	13:01:28	43.015	77.541	3.8	Mb	ISC	38	1.86	128	3.14	18.3
2006-11-20	15:37:29	43.026	77.094	4.7	Mb	ISC	61	1.94	151	3.14	19.2
2007-03-07	20:13:34	42.689	78.434	4	Mb	ISC	88	1.9	178	2.94	17.5
2007-04-28	19:41:35	43.005	78.172	4	Mb	NNC	67	2.14	157	6.01	40.3
2007-06-05	07:14:14	43.107	77.011	3.1	Mb	NNC	1	1.59	91	1.75	8.8
2007-10-09	16:00:41	42.935	77.802	4.9	Mb	ISC	283	1.21	13	1.36	5.2
2007-11-03	04:16:53	42.915	77.351	3.2	Mb	NNC	33	1.6	123	2.46	12.4
2008-05-13	20:36:46	42.971	77.399	3.6	Mb	IDC	41	1.6	131	2.71	13.6
2008-07-14	06:56:11	43.444	78.273	3.6	Mb	IDC	58	1.91	148	4.31	25.8
2008-09-17	19:37:34	43.505	78.600	3.6	Mb	ISC	80	1.62	170	2.25	11.4
2008-10-27	00:48:12	43.022	78.030	3.7	Mb	NNC	62	1.53	152	3.12	15
2009-01-19	16:15:51	42.920	77.488	3.8	Mb	NNC	80	1.78	170	2.36	13.2
2009-04-08	17:15:04	43.057	77.157	3.7	Mb	MOS	15	1.8	105	2.26	12.8
2009-04-28	03:09:52	42.924	78.171	3.5	Mb	IDC	65	1.77	155	3.8	21.1
2009-09-22	20:31:37	43.276	77.626	3.6	Mb	NNC	59	2.22	149	5.29	37
2009-11-04	09:28:41	42.948	78.209	3.6	Mb	IDC	67	2.24	157	4.89	34.3
2010-06-13	15:43:07	42.795	78.116	3.6	Mb	ISC	71	1.51	161	2.58	12.2
2010-12-23	16:04:49	42.982	78.175	3.6	Mb	IDC	63	1.35	153	1.86	7.9

Table A1. (continued)

Date	Origin Time	Latitude	Longitude	Magnitude	Magnitude Type	Magnitude Source	First Semiaxis (deg)	Length (km)	Second Semiaxis (deg)	Length (km)	Area (km^2)
2011-01-11	22:34:27	42.880	78.694	3.5	Mb	KRNET	84	1.53	174	1.99	9.6
2011-02-07	10:39:30	43.091	77.800	3.4	Mb	NNC	306	1.25	36	1.32	5.2
2011-02-16	06:53:10	43.120	78.167	3.1	Mb	NNC	291	1.58	21	1.9	9.4
2011-03-31	23:21:08	42.995	77.749	3.3	Mb	NNC	335	1.22	65	1.3	5
2011-04-01	04:12:17	43.110	77.297	3.5	Mb	KRNET	346	1.29	76	1.36	5.5
2011-06-19	07:17:40	43.135	77.459	3.4	Mb	NNC	348	1.23	78	1.36	5.3
2011-07-09	12:57:52	42.798	77.988	3.3	Mb	NNC	79	1.39	169	1.45	6.4
2011-11-18	10:45:22	43.300	78.116	3	Mb	NNC	289	1.34	19	1.65	7
2011-11-30	03:30:28	42.894	78.354	3.1	Mb	KRNET	68	1.39	158	2.76	12.1
2012-01-08	19:00:45	42.899	78.063	3.8	Mb	NNC	75	1.4	165	1.46	6.4
2012-04-15	02:56:06	42.931	77.870	3.6	Mb	KRNET	317	1.2	47	1.3	4.9
2012-05-17	06:01:45	42.852	78.512	3.9	Mb	ISC	359	1.42	89	1.43	6.4
2012-06-04	22:10:24	42.989	78.274	3.9	Mb	NNC	270	1.59	0	1.73	8.6
2012-06-12	08:20:22	42.813	77.968	3.5	Mb	KRNET	328	1.25	58	1.34	5.3
2012-06-18	21:07:42	43.060	77.575	3.6	Mb	KRNET	4	1.38	94	1.46	6.3
2012-10-12	07:18:47	43.060	78.212	3.7	Mb	KRNET	290	1.31	20	1.51	6.2
2012-12-05	00:57:15	43.114	78.317	4.1	Mb	ISC	275	1.3	5	1.34	5.5
2012-12-05	01:26:05	43.076	78.313	3.5	Mb	NNC	89	1.33	179	1.81	7.6

Unit 35 (paleosoil, pre-earthquake): This buried soil is about 10 cm thick, brown with clasts, and few roots. It is located between meters L and M and south of N and eroded and mixed into unit 30.

Unit 40 and 45 (alluvial sediment and paleosoil, footwall, pre-earthquake): a fine-grained alluvial sediment (unit 40), with a thin soil horizon preserved at its upper limit (unit 45). The paleosoil is in fault contact and overlain by the overturned forelimb of the hanging wall anticline, possibly thin brecciated horizon at the contact to folded gravel unit (unit 110). Both Units 40 and 45 are dark brown, clay, and silt rich with very few clasts and angular pebbles. *Samples*: B3 (bulk soil and radiocarbon).

Unit 100 to 120 (fluvial/alluvial gravel to cobble (100/110) and clay/silt (105/115) intercalations, pre-earthquake, hanging wall): The hanging wall comprises intercalations of mudflow (overbank) deposits with fluvial/alluvial gravel, pebble, and cobble. The clasts are mainly subrounded to subangular, mostly matrix supported and generally moderately sorted. The silty clay deposits are reddish brown and reach thicknesses of up to 20 cm. These layers of potential overbank deposits are more dominant in the lower half of the trench and comprise valuable markers to measure offset along secondary structures. Fossil snails exist mainly, but not solely, within these silty clay deposits. A channel has been incised into the upper part (120). *Samples*: C1-5 (charcoal and radiocarbon), S2-8, 10-21, and 23-25 (snails and radiocarbon).

Although this alluvial-fluvial sequence in principle comprises the same sediment package, it shows strong internal deformation that influences its appearance. Especially notably is a distinct change in texture and composition of the fluvial deposits between the northern and southern half (i.e., north and south of F2). The southern half is better sorted and clay beds are generally thinner. We interpret this as result of juxtaposition of different sediment packages by an oblique component. Furthermore, the hanging wall packages mimic the ramp structure that is only partly seen in the topography because of the thick pond sediments. In the following, we will differentiate four areas for structural details, i.e., A—north of F2; B—between F2 and H; C—between positions H and J; and D—south of J.

Subunit A: Gently NNW dipping (about 12°) units cut by several subparallel and subvertical cracks and faults with normal separation. Some cracks developed into open fissures near the surface. The cracks and secondary faults strike NE and dip with approximately 73° to SE, thus are parallel to the scarp at this location. The maximum observed (apparent) vertical separation was 30 cm; the cumulative normal offset across the trenched area of Subunit A sums up to about 66 cm.

Subunit B: Two major fissures, opened between conjugate sets of NE striking cracks that dip SE and NW, respectively, characterize this subarea. These fissures have a horizontal separation from about 1 m at the top to still about 10 cm at the trench bottom. Both fissures partly show rotated and aligned clasts along their

walls, collapse of fluvial material in the upper part and refilling with modern, organic-rich soil. Some oblique motion along the fissures, especially along F2, seems likely, as all but the lowest of the silty clay deposits stop abruptly at their position, the sediments south of F2 are better sorted, and a topographic break is associated with this position.

Subunit C: This sediment package has a slightly different textural appearance with smaller clasts, more compaction and thinner fine-grained intercalations. Bedding is tilted toward south (18°) and the few penetrating cracks mainly dip NW.

Subunit D: This package is separated from C by another penetrating crack and comprises the overturned forelimb of the hanging wall anticline that is thrust onto the footwall unit 40. The basal thrust, as measured below the anticline strikes N031°E, with a dip of 11°NW. The intercalations of coarser with finer facies clearly help to delineate the southwards steepening of the upper limb beds to about 36 to 40°. Carbonate coatings of cobbles and pebbles that are usually found at the undersides in an undisturbed setting mimic the folding and point to overturning at the base and in fault contact.

Appendix C: IRSL Protocols

C1. Sample Preparation and Instrumentation

Samples were prepared for coarse grain (90–250 μm) potassium feldspar (K-feldspar) analysis. In brief, this comprised HCl treatment to remove carbonates, H_2O_2 treatment to remove organics, wet sieving to the desired size fraction (150–250 μm) and density separation using "Fastfloat" to separate the K-feldspar grains ($<2.58\,g\,cm^{-3}$). This material was then etched in 10% HF for 15 min. All luminescence measurements were performed on a Risoe DA20 TL/OSL reader. Stimulation was provided by IR diodes (wavelength 870 nm) with detection of the resulting (blue violet) IRSL through a combination of Schott BG39 filters and Corning 7-59 filters (detection range 320–450 nm). Laboratory irradiation was performed using a calibrated (using Risoe calibration quartz) ^{90}Sr beta source with a dose rate at the time of measurement of $8.44\,Gy\,min^{-1}$.

C2. Environmental Dose Rate Determination

The total uranium, thorium, and potassium contents of the samples were determined from subsamples of the sampling tubes using inductively coupled plasma mass spectrometry at SGS laboratories, Vancouver, Canada. Elemental concentrations were converted to dose rates using the conversion factors of *Guérin et al*. [2011], with appropriate adjustment for grain size [*Mejdahl*, 1979; *Readhead*, 2002] and sample water content [*Aitken*, 1985]. Dose rates for internal K and Rb were based on the assumption of K-feldspar grain K and Rb concentrations of $12.5 \pm 0.5\%$ and 400 ± 100 ppm, respectively [*Huntley and Baril*, 1997; *Huntley and Hancock*, 2001]. It was assumed that the as-measured water content was appropriate and a 3% (absolute) uncertainty in water content was propagated into the final dose rate uncertainties. It is assumed that the dose rate remained constant for the duration of burial. Cosmic dose rates were determined following *Prescott and Hutton* [1994] and were based on the current sample burial depth.

C3. Equivalent Dose Determination

In light of the poor OSL properties of quartz in this region equivalent doses were determined for K-feldspars using the post-IR IRSL (pIRIR) single aliquot regeneration method [*Murray and Wintle*, 2000; *Thomsen et al*., 2008; *Buylaert et al*., 2009]. This approach is designed to minimize the malign effects of anomalous fading [*Huntley and Lamothe*, 2001] in K-feldspars and comprises an initial low temperature (50°C) IR stimulation followed by a high temperature (225°C) IR stimulation that accesses an electron population less affected by fading. The trade-off is that signal derived from the second IR stimulation tends to be less rapidly bleached on exposure to sunlight [*Colarossi et al*., 2015]. Analyses were conducted on small (2 mm) aliquots, containing ~200 grains. Growth curves were constructed using a saturating exponential fit in the "Analyst" software and the associated errors derived using a Monte Carlo simulation [*Duller*, 2007], incorporating an additional 1.5% systematic instrument error.

In this study the lower fading [i.e., *Buylaert et al*., 2012] $pIRIR_{290}$ protocol was not utilized as it was found to exhibit high residual doses (>26 Gy) and was not deemed appropriate in this setting (see below). The

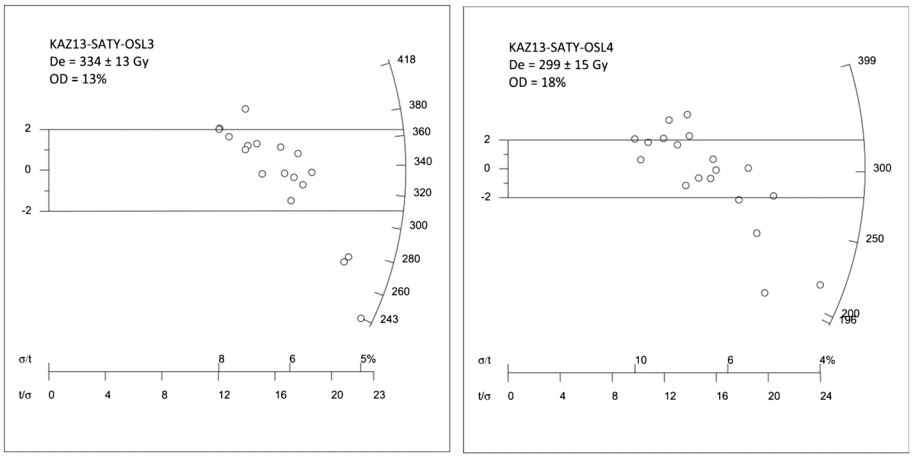

Figure C1. Radial plots illustrating the spread in measured pIRIR225 equivalent doses for the two SATY samples. The equivalent doses are read from the zero origin on the left, to the curved axis on the right. The precision of each individual equivalent dose measurement is indicated on the lower horizontal axis. The plots are centered on the central age model (CAM) equivalent dose estimate. The CAM equivalent doses and the overdispersion (OD) parameter are also reported.

$pIRIR_{225}$ signal was found to retain residual equivalent doses of 14.9 ± 1.4 Gy (SATY3) and 18.8 ± 3.9 Gy (SATY4) following 48 h of (Leicester) daylight exposure (April 2014), which amounted to 4% (SATY3) and 6% (SATY4) of the measured $pIRIR_{225}$ equivalent doses. Dose recovery experiments for the $pIRIR_{225}$ method conducted after an extended period of natural daylight exposure produced acceptable dose recovery ratios, with mean administered: measured ratios of 1.00 ± 0.02 (n = 6) for SATY3 and 0.96 ± 0.1 (n = 6) for SATY4. Both samples show growth in the sensitivity-corrected $pIRIR_{225}$ signal to > 500 Gy and the mean ratios of aliquot equivalent doses to the D_o parameter of the saturating exponential fit were 1.6 ± 0.3 and 1.4 ± 0.4 for SATY 3 and SATY 4 (respectively), well below the $2D_0$ value often used as cutoff for luminescence signal saturation. The samples responded well to the SAR protocol with recycling ratios consistently within 5% of unity and recuperation less than 0.5% of the natural sensitivity-corrected IRSL for all measured aliquots.

The $pIRIR_{225}$ equivalent dose distributions for the two samples are comparable in that they are both relatively broad and are slightly negatively skewed, with 2–3 low (200–250 Gy) D_e aliquots. As such, both samples also show some overdispersion (SATY3 = 13% and SATY4 = 18%). Equivalent doses and standard errors used for age estimation were therefore based on the central age model (CAM) [*Galbraith et al*., 1999], which includes the overdispersion in the equivalent dose standard error. A beta source calibration (3%) uncertainty is also folded into the final equivalent dose uncertainty.

Fading rates were estimated using a subset of aliquots from the equivalent dose determinations. Following *Auclair and Lamothe* [2003] the samples were preheated immediately after dosing and then stored for varying periods of time before measurement. The IR50 signal in both samples shows clear evidence of anomalous fading, with calculated g-values (% signal loss per "decade" of storage [*Aitken*, 1985]) of 4.8 ± 0.4% and 4.7 ± 0.8%. The interaliquot scatter in the IR50 fading rate measurements for SATY4 was also quite marked. The $pIRIR_{225}$ signal exhibited reduced, but not negligible fading rates, with calculated g-values of 2.3 ± 0.3 and 2.5 ± 0.6%. As before, SATY4 exhibited greater interaliquot variability in the measured fading rate. Given these measured fading rates the $pIRIR_{225}$ ages were corrected for fading following *Huntley and Lamothe* [2001]. This adds additional uncertainty to these ages. The resulting ages for the two samples are within uncertainties of one another and indicate depositional ages of 86–87 kyr (Table 3). These ages (and the uncorrected age estimates) are substantially greater than the anticipated postglacial age for T2. The issue of incomplete bleaching, particularly given the potentially short sediment transport distances at this site (Figure 4e) and the measured magnitudes of the residual signals cannot, at present, be ruled out [e.g., *Colarossi et al*., 2015]. In the absence of other chronological information for T2 at present, these ages are treated as maximum ages, pending further analysis (see Figure C1).

Acknowledgments

We thank all those involved in the 2013 field season, in particular, Ivan for safe and patient driving and Ainagul for her efficient camp management. We also thank the people and local council of Saty for their support throughout the fieldwork. We thank Ramon Arrowsmith for sharing his observations from field visits to the Kurmentey Mountains and Frank Krüger for making an advance copy of his manuscript on the 1889 earthquake available to us. Eric Bergman kindly gave advice on earthquake location procedures. KOMPSAT-2 imagery was obtained through a Category-1 award from the European Space Agency. Radiocarbon dating was funded through a grant from the UK National Centre for Earth Observation. The authors thank NERC for funding support through COMET+, EWF, and LICS. R.T.W. was funded by a University Research Fellowship from the Royal Society of London during the project duration. A.L. and C.H. were supported by the German Federal Ministry of Education and Research (sc 03G0809). Data for this paper are available by contacting the corresponding author at richard.walker@earth.ox.ac.uk. Individual author contributions are as follows: K.E.A., R.T.W., G.E.C., C.H., J.H., A. L., D.M., A.M., and M.R. all participated in the 2013 field campaign. Field logistics were organized by K.E.A. and A.M. A.L. and M.R. constructed the trench log. D.M. acquired and processed the aerial survey of the site, and A.E. interpreted the resulting digital topographic model. A.S.C. undertook infrared stimulated luminescence analyses. R.A.S. performed the earthquake relocations. All authors contributed to the text, which was compiled into the final manuscript by R.T.W. K.E.A. and R.T.W. were responsible for the overall scientific concept and project design.

References

Abdrakhmatov, K. Y., et al. (1996), Relatively recent construction of the Tien Shan inferred from GPS measurements of present-day crustal deformation rates, *Nature*, *384*, 450–453.

Aitken, M. J. (1985), *Thermoluminescence Dating*, 370 pp., Academic Press, London, Orlando.

Alinaghi, A., and F. Krüger (2014), Seismic array analysis and redetermination of depths of earthquakes in Tien-Shan: Implications for strength of the crust and lithosphere, *Geophys. J. Int.*, *198*(2), 1111–1129.

Arrowsmith, J. R., C. J. Crosby, A. M. Korjenkov, E. Mamyrov, I. Povolotskaya, B. Guralnik, and A. Landgraf (2015), Surface rupture of the 1911 Kemin (Chon-Kemin) earthquake, northern Tien Shan, Kyrgyzstan, in revision for "Seismicity, Fault Rupture and Earthquake Hazard in Slowly Deforming Regions", Geol. Soc. of London Spec. Publ.

Auclair, M., M. Lamothe, and S. Huot (2003), Measurement of anomalous fading for feldspar IRSL using SAR Radiation Measurements, *Radiat. Meas.*, *37*, 487–492.

Baljinnyam, I., et al. (Ed.) (1993), *Ruptures of Major Earthquakes and Active Deformation in Mongolia and Its Surroundings*, vol. 181, Geol. Soc. of Am. Boulder, Colo.

Besstrashnov, V. (1993), Report on the results of seismogeological investigations in the area of the Mainak water-power plant on the Charyn river, Hydroproject Association, Unpublished Report, in Russian.

Bindi, D., A. A. G. Capera, S. Parolai, K. Abdrakhmatov, M. Stucchi, and J. Zschau (2012), Location and magnitudes of earthquakes in Central Asia from seismic intensity data: Model calibration and validation, *Geophys. J. Int.*, doi:10.1093/gji/ggs039.

Blaser, L., F. Krüger, M. Ohrnberger, and F. Scherbaum (2010), Scaling relations of earthquake source parameter estimates with special focus on subduction environment, *Bull. Seismol. Soc. Am.*, *100*(6), 2914–2926.

Bogdanovich, K. I., I. M. Kark, B. Y. Korol'kov, and D. I. Mushketov (1914), Earthquake in Northern district of Tien-Shan, 22 December 1910 (4 January 1911), St. Peterburg, Russia, Commision of the Geology Committee, p. 250.

Bondár, I., S. C. Myers, E. R. Engdahl, and E. A. Bergman (2004), Epicentre accuracy based on seismic network criteria, *Geophys. J. Int.*, *156*(3), 483–496.

Buylaert, J. P., A. S. Murray, K. J. Thomsen, and M. Jain (2009), Testing the potential of an elevated temperature IRSL signal from K-feldspar, *Radiat. Meas.*, *44*, 560–565.

Buylaert, J. P., M. Jain, A. S. Murray, K. J. Thomsen, C. Thiel, and R. Sohbati (2012), A robust feldspar luminescence dating method for Middle and Late Pleistocene sediments, *Boreas*, *41*(3), 435–451.

Campbell, G. E., R. T. Walker, K. Abdrakhmatov, J. L. Schwenninger, J. Jackson, J. R. Elliott, and A. Copley (2013), The Dzhungarian fault: Late Quaternary tectonics and slip rate of a major right-lateral strike-slip fault in the northern Tien Shan region, *J. Geophys. Res. Solid Earth*, *118*, 5681–5698, doi:10.1002/jgrb.50367.

Campbell, G. E., R. T. Walker, K. Abdrakhmatov, J. Jackson, J. R. Elliott, D. Mackenzie, T. Middleton, and J. L. Schwenninger (2015), Great earthquakes in low strain rate continental interiors: An example from SE Kazakhstan, *J. Geophys. Res. Solid Earth*, *120*, 5507–5534, doi:10.1002/2015JB011925.

Chen, W.-P., and P. Molnar (1983), Focal depths of intracontinental and intraplate earthquakes and their implications for the thermal and mechanical properties of the lithosphere, *J. Geophys. Res.*, *88*(B5), 4183–4214, doi:10.1029/JB088iB05p04183.

Colarossi, D., Duller, G. A. T., Roberts, H. M., Tooth, S., Lyons, J. R. (2015), Comparison of paired quartz OSL and feldspar pIRIR dose distributions in poorly bleached fluvial sediments from South Africa, *Quat. Geochronol.*, doi:10.1016/j.quageo.2015.02.015, in press.

Crosby, C., J. Arrowsmith, A. Korjenkov, B. Guralnik, E. Mamyrov, and I. Povolotskaya (2007), The Hunt for Surface rupture from the 1889 Ms8.3 Chilik earthquake, Northern Tien-Shan, Kyrgyzstan and Kazakhstan, AGU Fall Meeting Abstracts, F5, Poster Presentation.

Davison, C. (1921), On scales of seismic intensity and on the construction and use of isoseismal lines, *Bull. Seismol. Soc. Am.*, *11*(2), 95–130.

Delvaux, D., K. E. Abdrakhmatov, I. N. Lemzin, and A. L. Strom (2001), Landslides and surface breaks of the 1911 Ms 8.2 Kemin earthquake, Kyrgyzstan, *Russian Geol. Geophys.*, *42*(10), 1583–1592.

Djanuzakov, K. D., Omuraliev, M., Omuralieva, A., Iliasov, B. I., Grebennikova, V. V. (2003), *Strong Earthquakes of the Tien-Shan* [in Russian], 215 pp., Ilim, Bishkek.

Duller, G. A. T. (2007), Assessing the error on equivalent dose estimates derived from single aliquot regenerative dose measurements, *Ancient TL*, *25*, 15–24.

Durcan, J. A., G. E. King, and G. A. T. Duller (2015), DRAC: Dose rate and age calculator for trapped charge dating, *Quat. Geochronol.*, *28*, 54–61.

Elliott, J. R., E. K. Nissen, P. C. England, J. A. Jackson, S. Lamb, Z. Li, M. Oehlers, and B. Parsons (2012), Slip in the 2010–2011 Canterbury earthquakes, New Zealand, *J. Geophys. Res.*, *117*, B03401, doi:10.1029/2011JB008868.

Elliott, J. R., A. J. Elliott, A. Hooper, Y. Larsen, P. Marinkovic, and T. J. Wright (2015), Earthquake monitoring gets boost from a new satellite, *Eos Trans. AGU*, *96*, 14–18.

England, P., and J. Jackson (2011), Uncharted seismic risk, *Nat. Geosci.*, *4*, 348–349.

Erzhanov, Z. S., K. E. Kalmurzaev, and I. L. Nersesov (1978), Dzhalanash-Tyup earthquake 25/03/1978, *Vestnik AS KazSSR*, *N10*, 38–44.

Field, E. H., et al. (2014), Uniform California Earthquake Rupture Forecast, Version 3 (UCERF3)—The Time-Independent Model, *Bull. Seismol. Soc. Am.*, *104*(3), 1122–1180.

Galbraith, R. F., R. G. Roberts, G. M. Laslett, H. Yoshida, and J. M. Olley (1999), Optical dating of single and multiple grains of quartz from Jinmium rock shelter, northern Australia, part 1, Experimental design and statistical models, *Archaeometry*, *41*, 339–364.

Ghose, S., R. J. Mellors, A. M. Korjenkov, M. W. Hamburger, T. L. Pavlis, G. L. Pavlis, M. Omuraliev, E. Mamyrov, and A. R. Muraliev (1997), The MS = 7.3 1992 Suusamyr, Kyrgyzstan, earthquake in the Tien Shan: 2. Aftershock focal mechanisms and surface deformation, *Bull. Seismol. Soc. Am.*, *87*(1), 23–38.

Guérin, G., N. Mercier, and G. Adamiec (2011), Dose-rate conversion factors: Update, *Ancient TL*, *29*, 5–8.

Hay, M. B. (1888), The earthquakes of May and June, 1887, in the Verny (Vernoe) District, Russian Turkestan, and their consequences, *Proc. R. Geogr. Soc. Mon. Rec. Geogr.*, *10*, pp. 638–646.

Hornblow, S., M. Quigley, A. Nicol, R. Van Dissen, and N. Wang (2014), Paleoseismology of the 2010 Mw 7.1 Darfield (Canterbury) earthquake source, Greendale Fault, New Zealand, *Tectonophysics*, *637*, 178–190.

Huntley, D. J., and D. J. Baril (1997), The K content of the K-feldspars being measured in optical dating or in thermoluminescence dating, *Ancient TL*, *15*, 11–13.

Huntley, D. J., and R. G. V. Hancock (2001), The Rb contents of the K-feldspars being measured in optical dating, *Ancient TL*, *19*, 43–46.

Huntley, D. J., and M. Lamothe (2001), Ubiquity of anomalous fading in K-feldspars and the measurement and correction for it in optical dating, *Can. J. Earth Sci.*, *38*, 1093–1106.

Johnson, K., E. Nissen, S. Saripalli, J. R. Arrowsmith, P. McGarey, K. Scharer, P. Williams, and K. Blisniuk (2014), Rapid mapping of ultrafine fault zone topography with structure from motion, *Geosphere*, *10*(5), 969–986.
Jordan, T. H., and K. A. Sverdrup (1981), Teleseismic location techniques and their application to earthquake clusters in the south-central Pacific, *Bull. Seismol. Soc. Am.*, *71*(4), 1105–1130.
Kalmetieva, Z., A. Mikolaichuk, B. Moldobekov, A. Meleshko, M. M. Jantaev, and A. V. Zubovich (2009), *Atlas of Earthquakes in Kyrgyzstan*, [of English version], edited by H. B. Havenith, Bishkek, CAIAG.
Krüger, F., G. Kulikova, and A. Landgraf (2015), Instrumental magnitude constraints for the 11 July 1889, Chilik earthquake, in *Seismicity, Fault Rupture and Earthquake Hazards in Slowly Deforming Regions*, vol. 432, edited by A. Landgraf et al., Geol. Soc. of London Spec. Publ.
Kulikova, G., and F. Krüger (2015), Source process of the 1911 M8.0 Chon-Kemin earthquake: Investigation results by analogue seismic records, *Geophys. J. Int.*, *201*(3), 1891–1911.
Kumar, S., S. G. Wesnousky, T. K. Rockwell, D. Ragona, V. C. Thakur, and G. G. Seitz (2001), Earthquake recurrence and rupture dynamics of Himalayan Frontal Thrust, India, *Science*, *294*(5550), 2328–2331.
Kumar, S., S. G. Wesnousky, T. K. Rockwell, R. W. Briggs, V. C. Thakur, and R. Jayangondaperumal (2006), Paleoseismic evidence of great surface rupture earthquakes along the Indian Himalaya, *J. Geophys. Res.*, *111*, B03304, doi:10.1029/2004JB003309.
Landgraf, A., A. Dzhumabaeva, K. Abdrakhmatov, E. A. Macaulay, M. R. Strecker, J. R. Arrowsmith, F. Preusser, G. Rugel, and S. Merchel (2016), Repeated large-magnitude earthquakes in a tectonically active, low-strain continental interior: The northern Tien Shan, Kyrgyzstan, *J. Geophys. Res. Solid Earth*, doi:10.1002/2015JB012714.
Manighetti, I., M. Campillo, S. Bouley, and F. Cotton (2007), Earthquake scaling, fault segmentation, and structural maturity, *Earth Planet. Sci. Lett.*, *253*(3), 429–438.
McNamara, D. E., H. M. Benz, R. Herrmann, E. Bergman, and M. Chapman (2014), The M_w 5.8 central Virginia seismic zone earthquake sequence of August 23, 2011: Constraints on earthquake source parameters and fault geometry, *Bull. Seismol. Soc. Am.*, *104*(1), doi:10.1785/0120130058.
Mejdahl, V. (1979), Thermoluminescence dating—Beta-dose attenuation in quartz grains, *Archaeometry*, *21*, 61–72.
Mellors, R. J., F. L. Vernon, G. L. Pavlis, G. A. Abers, M. W. Hamburger, S. Ghose, and B. Iliasov (1997), The Ms = 7.3 1992 Suusamyr, Kyrgyzstan, earthquake: 1. Constraints on fault geometry and source parameters based on aftershocks and body-wave modeling, *Bull. Seismol. Soc. Am.*, *87*(1), 11–22.
Murray, A. S., and A. G. Wintle (2000), Luminescence dating of quartz using an improved single-aliquot regenerative-dose protocol, *Radiat. Meas.*, *32*, 57–73.
Mushketov, I. V. (1890), The Verny Earthquake 28th May (9th June) 1887, Memoirs of the Geological Committee, 10(1), St Petersburg.
Mushketov, I. V. (1891), Materials for investigation of earthquakes in Russia, Annex to the 27th volume of tidings of the Imperial Russian Geographical Society.
Nersesov, I. L., A. Sydykov, A. Nurmaganbetov, and N. N. Michailova (1981), Seismic regime of North Tien Shan in connection with Dzhalanash-Tyup earthquake 25.03.1978, *Phys. Earth*, *5*.
Philip, H., E. Rogozhin, A. Cisternas, J. C. Bousquet, B. Borisov, and A. Karakhanian (1992), The Armenian earthquake of 1988 December 7: Faulting and folding, neotectonics and paleoseismicity, *Geophys. J. Int.*, *110*, 141–158.
Pigati, J. S., J. A. Rech, and J. C. Nekola (2010), Radiocarbon dating of small terrestrial gastropod shells in North America, *Quat. Geochronol.*, *5*, 519–532.
Prescott, J. R., and J. T. Hutton (1994), Cosmic ray contributions to dose rates for luminescence and ESR dating: Large depths and long-term variations, *Radiat. Meas.*, *23*, 497–500.
Quigley, M., R. Van Dissen, N. Litchfield, P. Villamor, B. Duffy, D. Barrell, K. Furlong, T. Stahl, E. Bilderback, and D. Noble (2012), Surface rupture during the 2010 M_w 7.1 Darfield (Canterbury) earthquake: Implications for fault rupture dynamics and seismic-hazard analysis, *Geology*, *40*(1), 55–58.
Readhead, M. L. (2002), Absorbed dose fraction for ^{87}Rb beta particles, *Ancient TL*, *20*, 25–29.
Reimer, P. J., et al. (2013), Selection and treatment of data for radiocarbon calibration: An update to the International Calibration (IntCal) criteria, *Radiocarbon*, *55*(4), 1923–1945.
Ritzwoller, M. H., N. M. Shapiro, A. L. Levshin, E. A. Bergman, and E. R. Engdahl (2003), Ability of a global three-dimensional model to locate regional events, *J. Geophys. Res.*, *108*(B7), 2353, doi:10.1029/2002JB002167.
Rizza, M., et al. (2011), Slip rate and slip magnitudes of past earthquakes along the Bogd left-lateral strike-slip fault (Mongolia), *Geophys. J. Int.*, *186*(3), 897–927.
Rizza, M., et al. (2015), Earthquake Geology of the Bulnay Fault (Mongolia), *Bull. Seismol. Soc. Am.*, *105*(1), 72–93.
Roustaei, M., E. Nissen, M. R. Abbassi, M. Ghorashi, A. Gholamzadeh, M. Tatar, F. Yamini-Fard, E. A. Bergman, J. A. Jackson, and B. E. Parsons (2009), Vertical separation of surface folding, earthquake faulting, and aftershocks in the Zagros Simply Folded Belt (Iran), *Geophys. J. Int.*, *142*, 1–24.
Selander, J., M. Oskin, C. Ormukov, and K. Abdrakhmatov (2012), Inherited strike-slip faults as an origin for basement-cored uplifts: Example of the Kungey and Zailiskey ranges, northern Tian Shan, *Tectonics*, *31*, TC4026, doi:10.1029/2011TC003002.
Sloan, R. A., J. A. Jackson, D. McKenzie, and K. Priestley (2011), Earthquake depth distributions in central Asia, and their relations with lithosphere thickness, shortening and extension, *Geophys. J. Int.*, *185*(1), 1–29.
Stein, S., and A. M. Friedrich (2014), How much can we clear the crystal ball?, *Astron. Geophys.*, *55*(2), 2–11.
Tapponnier, P., and P. Molnar (1979), Active faulting and Cenozoic tectonics of the Tien Shan, Mongolia, and Baykal regions, *J. Geophys. Res.*, *84*(B7), 3425–3459, doi:10.1029/JB084iB07p03425.
Tatar, M., J. Jackson, D. Hatzfeld, and E. Bergman (2007), The 2004 May 28 Baladeh earthquake (M_w 6.2) in the Alborz, Iran: Overthrusting the South Caspian Basin margin, partitioning of oblique convergence and the seismic hazard of Tehran, *Geophys. J. Int.*, *170*(1), 249–261.
Thompson, S. C., R. J. Weldon, C. M. Rubin, K. Abdrakhmatov, P. Molnar, and G. W. Berger (2002), Late Quaternary slip rates across the central Tien Shan, Kyrgyzstan, central Asia, *J. Geophys. Res.*, *107*(B9), 2203, doi:10.1029/2001JB000596.
Thomsen, K. J., A. S. Murray, M. Jain, and L. Botter-Jensen (2008), Laboratory fading rates of various luminescence signals from feldspar-rich sediment extracts, *Radiat. Meas.*, *43*, 1474–1486.
Tibaldi, A. (1998), Effects of topography on surface fault geometry and kinematics: Examples from the Alps, Italy and Tien-Shan, Kazakstan, *Geomorphology*, *24*(2), 225–243.
Tibaldi, A., E. Graziotto, F. Forcella, and V. Gapich (1997), Morphotectonic indicators of Holocene faulting in central Tien-Shan, Kazakstan, and geodynamic implications, *J. Geodyn.*, *23*(1), 23–45.
Walker, R. T., et al. (2006), Geomorphology and structure of the Jid right-lateral strike-slip fault in the Mongolian Altay mountains, *J. Struct. Geol.*, *28*(9), 1607–1622.

Walker, R. T., E. A. Bergman, W. Szeliga, and E. J. Fielding (2011), Insights into the 1968–1997 Dasht-e-Bayaz and Zirkuh earthquake sequences, eastern Iran, from calibrated relocations, InSAR and high-resolution satellite imagery, *Geophys. J. Int.*, *187*(3), 1577–1603.

Walker, R. T., et al. (2013), The 2010–2011 South Rigan (Baluchestan) earthquake sequence and its implications for distributed deformation and earthquake hazard in southeast Iran, *Geophys. J. Int.*, *193*(1), 349–374.

Walker, R. T., K. W. Wegmann, A. Bayasgalan, R. J. Carson, J. Elliott, M. Fox, E. Nissen, and R. A. Sloan (2015), The Egiin Davaa rupture, central Mongolia: A large-magnitude prehistoric normal faulting earthquake from a slowly-deforming continental interior, *Geol. Soc. London Spec. Publ.*, *432*, doi:10.1144/SP432.4.

Wesnousky, S. G. (2006), Predicting the endpoints of earthquake ruptures, *Nature*, *444*(7117), 358–360.

Westoby, M. J., J. Brasington, N. F. Glasser, M. J. Hambrey, and J. M. Reynolds (2012), 'Structure-from-Motion' photogrammetry: A low-cost, effective tool for geoscience applications, *Geomorphology*, *179*, 300–314.

Wilhelmson, P. M. (1947), Kemin-Chui Erdbeben, 21 Juni, 1938. Proceedings of the National Academy of Science of Kazakhstan, Almaty, Kazakhstan, 39 pg.

Zubovich, A. V., et al. (2010), GPS velocity field for the Tien Shan and surrounding regions, *Tectonics*, *29*, TC6014, doi:10.1029/2010TC002772.